Journal of Computational Physics **152,** 517–549 (1999)
Article ID jcph.1999.6238, available online at http://www.idealibrary.com on IDEAL®

Large-Eddy Simulation of the Shock/Turbulence Interaction

F. Ducros,* V. Ferrand,*,† F. Nicoud,*,[1] C. Weber,* D. Darracq,* C. Gacherieu,* and T. Poinsot*,†

*CERFACS, Centre Européen de Recherche et de Formation Avancée en Calcul Scientifique, 42, Avenue Gaspard Coriolis, 31057 Toulouse Cedex, France; †IMFT, Institut de Mécanique des Fluides de Toulouse, Allee du Professeur Camille Soula, 31400 Toulouse, France
E-mail: ducros@cerfacs.fr

Received April 30, 1998; revised February 4, 1999

The objective of this work is to derive a shock capturing tool able to treat turbulence with minimum dissipation out of the shock for a large-eddy simulation (LES) of the shock/turbulence interaction. The present numerical modeling of the shock/turbulence interaction consists of a second-order finite volume central scheme using a skew-symmetric form, a Jameson's type artificial dissipation, and the filtered structure function model. We focus on two areas to build simulations of increased accuracy:

- A new sensor for triggering artificial dissipation is developed to perform LES of the shock/turbulence interaction. This sensor is simple, local, and does not require any a priori knowledge of the shock position. It is first tested in freely decaying turbulence for both viscous and inviscid cases and in the inviscid 2D vortex/shock interaction. It is shown that both shock capturing properties and standard LES results in the case of freely decaying turbulence are recovered.
- Even though this modified sensor limits dissipation away from the shock, it is shown that the dissipation used inside the shock affects turbulence when eddies cross the shock region. This effect can be minimized by (1) refining the mesh in the vicinity of the shock or (2) pre-filtering. The results obtained by mesh refinement are investigated for the inviscid shock/turbulence interaction in terms of Reynolds stresses and kinetic energy variations accross the shock. A priori testing shows that, with the proposed scheme and for all meshs considered, the dominant dissipation acting on kinetic energy is the SGS dissipation away from the shock and both artificial and SGS dissipation in the shock, the former being larger than the latter.

Key Words: large-eddy simulation; numerical viscosity; compressible flow; subgrid-scale model; shock/turbulence interaction.

[1] Present address: Center for Turbulence Research, Stanford University.

0021-9991/99 $30.00

1. INTRODUCTION

The interaction of shock waves and turbulence is common in high speed flows, and of particular aerodynamic interest (buffeting, air intakes,...). Many studies and results are available on this subject, extending from experimental ([1–3] for interaction of turbulent boundary layer and shock) to theoretical [4, 5] and numerical fields [6–9]. As underlined in Lee *et al.* [6], the general finding is that both shock and turbulence are modified during their interaction: the shock is corrugated, depending on the level of turbulence, whereas turbulence intensities and Reynolds stresses are amplified across the shock wave. As far as turbulence length-scales are concerned, a general consensus arises considering that small scales are more amplified than the large ones, leading to a global decrease of the Taylor microscale (referred to as length scale, see [6] for details and [10, 11] for a contradictory debate).

For wall bounded flows, Reynolds average Navier–Stokes (RANS) equations may be used for flows where the shock does not induce separation [12, 13]. For separated flows, however, only unsteady calculations of shock/turbulence interaction may provide a realistic description of the flow. In this context, unsteady RANS can provide encouraging results as shown by Soulères [14] for strong buffeting occurring on an airfoil. However, standard RANS models cannot describe turbulent field jumps through the shock and therefore are to be modified. Such simulations are developed with different motivations, focusing either on the shock-capturing techniques [15], or on the description of large coherent structures of turbulence via large-eddy simulation (see [16, 17]).

Another trend is to make use of dissipative numerical methods to treat both turbulence and strong discontinuities for unsteady applications: this leads to encouraging results in terms of turbulence modeling when using the piecewise parabolic method, for example (see [18–20]) or the so-called monotonic integrated LES (MILES) approach. However, other studies comparing true SGS and numerical dissipation show that the latter overcomes the former one in some cases [21]: this may be due to the fact that classical shock-capturing schemes reduce to first order in the shock. Moreover, built-in numerical dissipation is unable to vanish in near-wall regions as SGS dissipation does, which can be seen as a major drawback of the MILES approach and may limit their applications to free shear flows whereas the present method may be seen as more general.

Fundamental work on numerical simulation of the shock/grid-generated-turbulence interaction is now developing, the aim of which is to understand more precisely the mechanisms by which turbulence interacts with shock waves. This is done through direct numerical simulations (DNS) based on the complete resolution of the shock for relatively low incident Mach numbers [7, 22, 13] or with shock capturing techniques [6]. High order schemes (typically compact schemes of 6th order) are commonly used for these DNS, for which the upstream Mach number M_1 ranges from 1.05 to 2, the turbulent Mach number M_t between 0.05–0.102, and the turbulent Reynolds number Re_t between 84 and 240 for a Taylor microscale Reynolds number Re_λ between 6 and 20. The use of shock capturing techniques (sixth order ENO schemes [6]) allows increasing M_1 up to 3. For this latter work, turbulent scales are simulated explicitly, whereas the shock is captured using a mesh size 7 times larger (in the shock-normal direction) than the mesh size required to perform the equivalent DNS. For this work, Lee *et al.* [6] and Mahesh *et al.* [8] make use of the concept of "local application of the ENO scheme," which limits the application of the ENO scheme in two ways: first it applies only in a direction normal to the undisturbed shock and second it is

limited to a zone surrounding the shock which covers only 10% of the calculation domain. This may be done only because both the direction and the shock position are known a priori. This concept was necessary for two reasons: first to permit a cost reduction (the ENO reconstruction is computationally expensive) and second to limit the extra dissipation brought up by the numerical dissipation inherent to the upwinding. These simulations recover the main features of shock/turbulence interaction, even if some discrepancies between linear interaction analysis (LIA) of Ribner [4] and numerical predictions appear, mainly due to viscous decay. An appropriate compensation makes these DNS results consistent with the LIA approach [6, p. 233]. Despite the high-order of the method, Lee *et al.* [6] suggest that the local refinement of the mesh in the direction normal to the shock is required in order to describe the thermodynamic fluctuations due to the shock. We shall come back to this point hereafter.

A preparatory work toward LES of fundamental shock/turbulence interaction has been also reported [23]. The underlying numerical method used for this work is again a local ENO scheme, together with the compressible dynamic model of [24]. However, if the methodology followed by these previous works matches the classical numerical requirement for LES (use of high order schemes, see [25, 26]), some aspects of the solution proposed prevent a direct extension to more complex geometries. First, these treatments will fail when the shock is not aligned with the mesh, or when the shock moves. Second, the extension of an intrinsically dissipative discontinuity capturing scheme may not be able to be generalized to the whole domain of calculation for LES [27], even if such high-order schemes clearly exhibit some subgrid scale model behaviour.

The primary objective of this work is to derive a numerical tool devoted to LES of the shock/turbulence interaction for application in complex geometries: we address the problem of compatibility for a numerical scheme between sufficient dissipation in the shock to capture the discontinuity and minimum dissipation far from the shock (less than the eddy viscosity model). After a description of the subgrid scale parametrization retained for these weakly compressible LES in Section 2, we present the numerical tool in Section 3. The results obtained for freely decaying isotropic compressible turbulence and for the 2D shock/vortex interaction are shown in Subsections 4.1 and 4.2, whereas those obtained for the shock/turbulence interaction are described in Subsection 4.3. A priori tests on relative numerical and SGS dissipations are provided in Subsection 4.4. These results are discussed in Section 5 where the importance of the ratio of the filter size to the smallest energetic turbulent scales is emphasized.

2. COMPRESSIBLE LES MODELING

The objective of the present study is to treat weakly compressible isotropic turbulence in the presence of a strong discontinuity. We provide a brief review of the state of the art for compressible LES modeling before describing our method.

As recalled in Lele [28], compressibility effects on turbulence are measured by the turbulent Mach number $M_t = \sqrt{q}/c$, where q is the turbulence kinetic energy and c the sound velocity, and by the ratio of compressible to solenoidal energy χ. Although a priori tests conducted on DNS of compressible turbulence suggest that the contribution of the trace of the subgrid scale tensor may be neglected [29], other works propose a model for this trace, either based on original work [30], or on an analog of Bardina's model [31] or on the dynamic procedure of Germano [24]. In this last work, Moin and co-workers show

that, for high Reynolds numbers and turbulent Mach numbers about $M_t \approx 0.3$, the dynamic coefficient brought up by the modeling of the trace of the subgrid scale tensor can exceed the dynamic coefficient obtained for its anisotropic part: this finding is followed by the fact that the gradients of resolved pressure and of SGS kinetic energy are of the same order [24, 32]. This result can be of great importance for the present study since it is known that the pressure work is the main contributor to the increase of the turbulence kinetic energy just downstream of the shock wave [7].

Despite these studies, we choose a subgrid scale modeling that does not take into account the possible contribution of the trace of the subgrid scale tensor. This crude modeling has already produced good results over a similar range of turbulent Mach numbers [33, 34] and we limit our work to turbulence at high Reynolds numbers and low turbulent Mach number ($M_t \approx 0.075$ upstream of the shock) away from shock regions. Moreover, following Morkovin's hypothesis, which is valid away from shock regions, this leads to a very weak level of compressible effects at small scale [35]. This will be confirmed by the very low level of the quantity $\Xi(\mathbf{x}) = \sqrt{\Theta'^2}(\mathbf{x})/\sqrt{\omega'^2}(\mathbf{x})$ registered in these regions, which measures the relative level of dilatation fluctuations $\sqrt{\Theta'^2}$ to the vorticity fluctuations $\sqrt{\omega'^2}$ (i.e., the relative level of compressible to incompressible velocity fluctuations, Ξ being proportional to χ, see [36, 28]). In the region of the shock, the SGS dissipation will be shown to be overwhelmed by the numerical dissipation (see the end of the paper), leading to a weaker importance of the model, at least for the present numerical procedure. Classical approaches for LES rely on the filtering of the fields by a filter $\bar{}$ due to the mesh and the discretization technique and a filter $\tilde{}$ which stands for its Favre-filtering counterpart (see [24, 31, 32]). The filters implicitly involve a cutoff length scale $\Delta_c \approx 2\Delta$, which classically corresponds to a spectral cutoff wavenumber $k_c \approx \pi/\Delta$ (Δ is a measure of the step size and could therefore depend on location, $\Delta = \Delta(\mathbf{x})$, and on direction). The resolved scales extend from the larger (which scale with the domain size) to the smallest (L_{uvw}, of wavelength k_{uvw}), which depend on the local state of the flow and are limited by the local cutoff length scale of the mesh: one gets $L_{uvw}(\mathbf{x}) \geq \Delta_c(\mathbf{x})$. The numerical requirements to capture strong discontinuities lead to the use of conservative variables ($\bar{\rho}$, $\bar{\rho}\tilde{u}_i$, $\bar{\rho}\tilde{e}$) where $\tilde{e} = C_v\tilde{T} + \tilde{u}_i\tilde{u}_i/2$.

This leads to the following set of non-dimensional equations,

$$\frac{\partial \bar{\rho}}{\partial t} + \frac{\partial \bar{\rho}\tilde{u}_j}{\partial x_j} = 0 \tag{1}$$

$$\frac{\partial \bar{\rho}\tilde{u}_i}{\partial t} + \frac{\partial \bar{\rho}\tilde{u}_i\tilde{u}_j}{\partial x_j} = -\frac{\partial \bar{p}}{\partial x_i} + \frac{\partial \mu\tilde{S}_{ij}}{\partial x_j} - \frac{\partial \tau_{ij}}{\partial x_j} \tag{2}$$

$$\frac{\partial \bar{\rho}\tilde{e}}{\partial t} + \frac{\partial \bar{\rho}\tilde{e}\tilde{u}_j}{\partial x_j} = -\frac{\partial \bar{p}\tilde{u}_j}{\partial x_j} + \frac{\partial(\mu\tilde{S}_{ij} - \tau_{ij})\tilde{u}_i}{\partial x_j} + \frac{\partial}{\partial x_j}\left(\lambda\frac{\partial \tilde{T}}{\partial x_j}\right) - \frac{\partial Q_j}{\partial x_j}, \tag{3}$$

where the subgrid scale tensor $\tau_{ij} = -\bar{\rho}\tilde{u}_i\tilde{u}_j + \overline{\rho u_i u_j}$ and the subgrid scale vector $Q_j = -\bar{\rho}C_p\tilde{u}_j\tilde{T} + \overline{\rho C_p u_j T}$ require modeling. The set of equations is closed by setting $\tau_{ij} - (1/3)\tau_{kk}\delta_{ij} = -\mu_t\tilde{S}_{ij}$ (μ_t is a eddy viscosity), where $\tilde{S}_{ij} = [\partial\tilde{u}_j/\partial x_i + \partial\tilde{u}_i/\partial x_j - (2/3)(\boldsymbol{\nabla}\cdot\tilde{\mathbf{u}})\delta_{ij}]$, $Q_i = -\bar{\rho}C_v\kappa_t(\partial\tilde{T}/\partial x_i)$ (κ_t is a eddy diffusivity), and by the modified filtered state equation $\bar{p} = \bar{\rho}R\tilde{T}$ (see [37, 34] for details). The explanations for the classical simplifications concerning the treatment of the filtered viscous terms in momentum and energy eqations and of the pressure-dilatation are given in [29, 24]. Once again, we assume that these simplifications hold for regions far from the shock, the shock regions being dominated by numerical dissipation: this hypothesis will receive some support in Subsection 4.4. The model

chosen for μ_t is the filtered structure function model [38, 39]. For this model, $\mu_t = \bar{\rho}\nu_t$ is evaluated as

$$\nu_t(\mathbf{x}, t) = 0.0014 C_K^{-3/2} \Delta(\mathbf{x}) [\tilde{F}_2(\mathbf{x}, \Delta, t)]^{1/2}, \tag{4}$$

where $\tilde{F}_2$ is a structure function evaluated on high pass filtered fields and $\Delta(\mathbf{x}) = (\mathcal{V}ol(\mathbf{x}))^{1/3}$, $\mathcal{V}ol(\mathbf{x})$ being the volume of the cell. The eddy diffusivity $\kappa_t = \nu_t / Pr_t$ is simply evaluated through a constant value of the turbulent Prandtl number Pr_t equal to 0.6, as recommended in [40] for passive scalar. Although this approximation is neither supported by the hypothesis of passive scalar for temperature in compressible turbulence, nor by the results of [24], we chose it for its simplicity in this first approach.

3. NUMERICAL TOOL

The numerical platform employed for the simulation is routinely used for steady aerodynamic calculations of industrial interest and is the Navier–Stokes multi-block parallel flow solver NSMB [41, 12]. For the present study where unsteady calculations are considered, the underlying numerical method consists of an explicit finite volume second-order centered scheme, augmented with a blending of second- and fourth-order artificial dissipation [42] for the space discretization. A four-stage Runge–Kutta scheme is used for time advancement. The code has been modified to take into account the subgrid scale modeling described in the previous section. The set of Eqs. (1) to (3) is reformulated to make classical fluxes F_i appear and reads

$$\frac{\partial \bar{U}}{\partial t} = \frac{\partial \bar{F}_1}{\partial x_1} + \frac{\partial \bar{F}_2}{\partial x_2} + \frac{\partial \bar{F}_3}{\partial x_3} \tag{5}$$

with

$$\bar{U} = {}^T(\bar{\rho}, \bar{\rho}\tilde{u}_1, \bar{\rho}\tilde{u}_2, \bar{\rho}\tilde{u}_3, \bar{\rho}\tilde{e}), \tag{6}$$

$$\bar{F}_i = F_i(\bar{U}) = \begin{pmatrix} -\bar{\rho}\tilde{u}_i \\ -\bar{\rho}\tilde{u}_i\tilde{u}_1 - \bar{p}\delta_{i1} + \mu(\tilde{T})\tilde{S}_{i1} - \tau_{i1} \\ -\bar{\rho}\tilde{u}_i\tilde{u}_2 - \bar{p}\delta_{i2} + \mu(\tilde{T})\tilde{S}_{i2} - \tau_{i2} \\ -\bar{\rho}\tilde{u}_i\tilde{u}_3 - \bar{p}\delta_{i3} + \mu(\tilde{T})\tilde{S}_{i3} - \tau_{i3} \\ -\tilde{u}_i(\bar{\rho}\tilde{e} + \bar{p}) + \mu(\tilde{T})\tilde{u}_j\tilde{S}_{ij} + \lambda(\tilde{T})\frac{\partial \tilde{T}}{\partial x_j} - \tilde{u}_j\tau_{ij} - Q_i \end{pmatrix}. \tag{7}$$

The standard Jameson's scheme involves a numerical flux at the interface between cells j and $j+1$

$$F_{j+1/2} = F\left(\frac{U_{j+1} + U_j}{2}\right) - d_{j+1/2}, \tag{8}$$

where

$$d_{j+1/2} = \epsilon^{(2)}_{j+1/2}(U_{j+1} - U_j) - \epsilon^{(4)}_{j+1/2}(U_{j+2} - 3U_{j+1} + 3U_j - U_{j-1}), \tag{9}$$

with

$$\epsilon^{(2)}_{j+1/2} = k^{(2)}\mathcal{R}_{j+1/2}\Psi_{j+1/2}, \tag{10}$$

$$\epsilon^{(4)}_{j+1/2} = \max\left(0.0, k^{(4)}\mathcal{R}_{j+1/2} - \epsilon^{(2)}_{j+1/2}\right). \tag{11}$$

$k^{(2)}$ and $k^{(4)}$ are real numbers fixing the amount of diffusion brought up by the second- and fourth-order dissipative operators. $\mathcal{R}_{j+1/2}$ is the spectral radius of the jacobian matrix $\partial F/\partial U$ at the cell face $j + 1/2$, measuring the anisotropic scaling factor of Swanson and Turkel [43]. $\Psi_{j+1/2}$ is a sensor based on pressure fluctuations

$$\Psi_j = \left|\frac{\bar{p}_{j+1} - 2\bar{p}_j + \bar{p}_{j-1}}{\bar{p}_{j+1} + 2\bar{p}_j + \bar{p}_{j-1}}\right|, \tag{12}$$

$$\Psi_{j+1/2} = \max(\Psi_j, \Psi_{j+1}). \tag{13}$$

The pertinence of the choice of a sensor based on the pressure gradient to treat shock discontinuities usually found in aerodynamics is discussed in [43]. Equations (5)–(13) refer to the classical Jameson scheme as described in [42]. It should be noted that the order of the artificial dissipation is the same as the order of the SGS dissipation and that both are non-linear, their non-linearities coming from coupling with either compressibility or turbulent state of the flow. This is why both are needed: the SGS dissipation being unable to sustain density and pressure discontinuities. It is admitted, within the LES community, that representative LES require high-order schemes [25]. Although Ghosal's analysis seems to disqualify second-order methods, it is worth noting that:

- Low order methods are common within applications in complex geometries, even for LES applications (see [44], for example).
- The presented skew-symmetric schemes are centered in nature, hence non-dissipative. Therefore the dissipation brought up by the model is effective. This fact will clearly appear under Results.
- Aliasing and dispersion errors, although being the potential cause of low quality results, cannot be responsible for the problems we will deal with. In that respect, the present problem and the proposed improvements will certainly hold for the use of an higher-order centered scheme.

Eventually, the form we adopt differs from the standard purely centered schemes by three features:

- First, as suggested by the analysis of Swanson and Turkel [43], the previous type of centered numerical method may be transformed into a TVD scheme by redefining the sensor (13), considering a matrix dissipation model instead of a scalar one as described in Eqs. (8) and (9), and setting the number $k^{(2)}$ to a value switching from central to first-order upwind scheme when second-order dissipation is activated. Although we keep a scalar dissipation model, we take the value $k^{(2)}$ equal to 1.5 which can be considered as large. As noticed in [43], a typical value around 0.5 gives a global scheme close to a first-order upwind scheme in the case of the scalar equation provided $k^{(2)}\Psi$ is equal to 0.5. For the presented test case, Ψ values are typically around 0.15, which leads to $k^{(2)}\Psi \approx 0.075$ for standard $k^{(2)} = 0.5$. This produces good results for stationary problems (RANS approach) but can lead to spurious oscillations in the shock region for the unsteady case. Empirically, we checked

that $k^{(2)}\Psi \approx 0.25$ (i.e., half the theoretical value recommended to get a true upwind scheme) is sufficient to suppress the above mentionned oscillations. The corresponding value for $k^{(2)}$ is 1.5. Following [43], this ensures a nearly TVD-like scheme in regions of sharp pressure gradient, and therefore offers the possibility to capture shocks without spurious oscillation. Fourth-order dissipation is used to damp high-frequency modes developing in all centered schemes even in smooth regions of the fluid flow field [42, 43]. For the present study, the value $\epsilon^{(4)}$ can be set to zero for two reasons. The first is that possible oscillations are damped by the LES model because they develop at small scales. The second reason is given below.

- Second, we detail some features of the chosen fluxes. Let us consider the non-linear equation

$$\frac{\partial U}{\partial t} + \frac{\partial U\psi}{\partial x} = 0, \tag{14}$$

ψ and U are scalars. The conservative discretization of the flux $(FU) = U\psi$ involved in Eq. (14) in a finite volume method based on collocated variables leads to the semi-discrete equation

$$\frac{\partial U}{\partial t} + \frac{F_{j+1/2} - F_{j-1/2}}{\mathcal{V}} = 0, \tag{15}$$

where $F_{j+1/2}$ is the flux at the interface $j+1/2$ between cells j and $j+1$, equal to $\psi U \cdot \mathbf{S}$, $\mathbf{S}$ being the normal at the cell surface. Using the mean value of the fluxes to evaluate $F_{j+1/2}$, one gets, in case of a regular mesh,

$$F_{j+1/2} = \frac{1}{2}(U_j\psi_j + U_{j+1}\psi_{j+1}) = \frac{1}{2}(F_j + F_{j+1}) \tag{16}$$

$$F_{j-1/2} = \frac{1}{2}(U_{j-1}\psi_{j-1} + U_j\psi_j) = \frac{1}{2}(F_{j-1} + F_j) \tag{17}$$

$F_j = U_j\psi_j$. The projection of Eq. (15) on $\mathbf{x}$ gives (with $\mathbf{S}\cdot\mathbf{x}/\mathcal{V} = \Delta_x^{-1}$)

$$\frac{\partial U}{\partial t} + \frac{U_{j+1}\psi_{j+1} - U_{j-1}\psi_{j-1}}{2\Delta x} = 0, \tag{18}$$

which is a semi-discrete equation of divergence form using a centered scheme of second-order in space. When using the flux of the mean value, one gets

$$F_{j+1/2} = F(U_{j+1/2}) = \left(\frac{U_j + U_{j+1}}{2}\right)\left(\frac{\psi_j + \psi_{j+1}}{2}\right) \tag{19}$$

$$F_{j-1/2} = F(U_{j-1/2}) = \left(\frac{U_{j-1} + U_j}{2}\right)\left(\frac{\psi_{j-1} + \psi_j}{2}\right) \tag{20}$$

which leads to

$$\frac{\partial U}{\partial t} + \frac{1}{2}\left(\frac{U_{j+1}\psi_{j+1} - U_{j-1}\psi_{j-1}}{2\Delta x}\right) + \frac{1}{2}U_j\left(\frac{\psi_{j+1} - \psi_{j-1}}{2\Delta x}\right) + \frac{1}{2}\psi_j\left(\frac{U_{j+1} - U_{j-1}}{2\Delta x}\right) = 0, \tag{21}$$

which is a semi-discrete equation using a skew-symmetric form of second-order. This form is known to reduce the aliasing errors that are crucial in low-order non-dissipative schemes and is thus recommended for LES (see [26, 32]). As pointed out in [45, 26], the skew-symmetric form is shown also to conserve kinetic energy for incompressible flows. Another interesting point is that the skew-symmetric form of Eq. (21) is compatible with the conservative discretization of Eq. (15), a property of crucial importance to ensure the shock capturing capability of the scheme. The adaptation to compressible flows with $\rho u_i u_j$ terms is made by setting U_j (respectively ψ_j) to $\overline{\rho}\tilde{u}_j$ (respectively $\overline{\rho}\tilde{u}_j$) in the form (21), the local flux $F_{j-1/2}$ of Eq. (20) being divided by the mean density $(\overline{\rho}_j + \overline{\rho}_{j+1})$.

• Third, as suggested in many applications devoted to steady (see Swanson, and Turkel [43] and Crumpton and Shaw [46]) or unsteady flow calculations (see Mittal [47]) there are strong motivations for reducing the second-order numerical dissipation used to capture discontinuities. Among them, the problem of shock wave representation is one of the strongest. Usual procedures to improve this dissipation rely either on a better mathematical description of TVD properties of the scheme [43], or on possibilities of reducing the size of the flow regions where dissipation acts: this is done in a very pragmatic way in fundamental studies where the concept of local application of ENO schemes arises [6] or by adding a correction to the sensor described in Eq. (9). Classical solutions are the use of a quantity having the same functional dependence as entropy, or the multiplication of the scaling factor by a monotonically increasing function of the local Mach number of the flow [43]. This latter procedure has been extended by [46] who directly flagged what is defined as the "shock region" before running every Runge–Kutta step: the flag is set to one in cells that are crossed by the shock front and to zero elsewhere.

As stressed by one of the referees, the Jameson scheme is no longer Galilean invariant due to the artificial viscosity, the range of values given for the coefficients $k^{(2)}$, $k^{(4)}$ being thus valid for the shock frame of reference. Moreover, with corrections based on the local Mach number, the discretized set of equations contains a new source on non-Galilean invariance. We developed a new correction which conserves the Galilean invariant property of the sensor and exhibits a smooth correction, proportional to the level of local compressibility. A modified version of the Jameson's sensor was obtained by multiplying the standard sensor Ψ of Eq. (12) by the local function Φ defined by

$$\Phi = \frac{(\boldsymbol{\nabla}\cdot\mathbf{u})^2}{(\boldsymbol{\nabla}\cdot\mathbf{u})^2 + (\boldsymbol{\omega})^2 + \epsilon}, \tag{22}$$

where $\boldsymbol{\omega} = \boldsymbol{\nabla}\wedge\tilde{\mathbf{u}}$ is the resolved vorticity and $\epsilon = 10^{-30}$ is a positive real number chosen to prevent numerical divergence in regions where both $\boldsymbol{\nabla}\cdot\mathbf{u}$ and $\boldsymbol{\omega}$ are zero. This function varies between 0 for weakly compressible regions to about 1 in shock regions. The artificial viscosity used with this "modified Jameson's approach" is

$$\epsilon^{(2)}_{i+1/2} = k^{(2)}\mathcal{R}_{i+1/2}\Psi_{i+1/2}\Phi_{i+1/2}, \tag{23}$$

where

$$\Psi_{i+1/2}\Phi_{i+1/2} = \max(\Psi_i\Phi_i, \Psi_{i+1}\Phi_{i+1}), \tag{24}$$

Ψ_i is given by Eqs. (13) and Φ_i is simply a local evaluation of Eq. (22). Note that, even though the Φ sensor of Eq. (22) is Galilean invariant and may be used in other numerical

formulations, its use with the Jameson scheme still leads to a non-Galilean invariant formulation. Therefore, present results (for example, constant $k^{(2)}$) should be extrapolated only in frames where shocks are steady.

4. RESULTS

The following numerical tests enable comparisons between numerical models for unsteady calculations of compressible flows, all of them involving the second-order finite volume centered scheme in the skew-symmetric form of Section 3.

For all simulations presented below, a dedicated table recalls the resolution, the values of the coefficients $k^{(2)}$ and $k^{(4)}$, the choice of the sensor Ψ or $\Phi\Psi$, and the eventual use of the LES model (referred to as FSF for the previously mentioned LES modeling).

We present simulations for both infinite and finite Reynolds numbers. The Euler simulations allow us to evaluate the numerical method in an inviscid case, all the dissipation being brought either by the artificial viscosity or/and by the SGS model. Experimental data of Comte-Bellot and Corrsin (CBC) were used for comparisons.

4.1. Homogeneous Compressible Turbulence

Models are first tested without shock in freely decaying homogeneous compressible turbulence in a periodic square box. Nine simulations are performed for different combinations of numerical and subgrid scale dissipation models (Table I). For the first six simulations (referred from THI-1 to THI-6), the initial condition consists in a divergence-free velocity field, with uniform initial density and temperature fields. The energy of the initial purely solenoidal velocity field is contained in the large resolved scales and peaks up at $k_i L_{ref} = 3$. For the three remaining simulations (referred from CBC-1 to CBC-3), the initial conditions consist of a divergence-free velocity field with the same three-dimensional energy spectrum as in the Comte-Bellot and Corrsin experiment at the station $tU_0/M = 42$ (see [48, 24]).

The resolution is low (32^3) but sufficient for the present goal. For the first four simulations, the kinetic energy spectra $E(k, t)$ fill up, showing transition to fully developed turbulence,

TABLE I
Parameters of Simulations for Three Dimensional Freely Decaying Isotropic Turbulence in a Periodic Square Box Using 32^3 Mesh Nodes

Simulation	FSF model	k^2	k^4	Sensor
THI-1	Yes	0.0	0	No sensor
THI-2	Yes	1.5	0.02	Ψ (Eq.13)
THI-3	Yes	1.5	0	Ψ
THI-4	Yes	1.5	0	$\Phi\Psi$ (Eq. 24)
THI-5	No	0.0	0	No sensor
THI-6	No	1.5	0	$\Phi\Psi$
CBC-1	Yes	0.0	0	No sensor
CBC-2	Yes	1.5	0	$\Phi\Psi$
CBC-3	Yes	1.5	0.02	Ψ

Note. THI-*x* refers to inviscid simulations: CBC-*x* refers to the Comte-Bellot and Corrsin experiment (see Subsection 4.1).

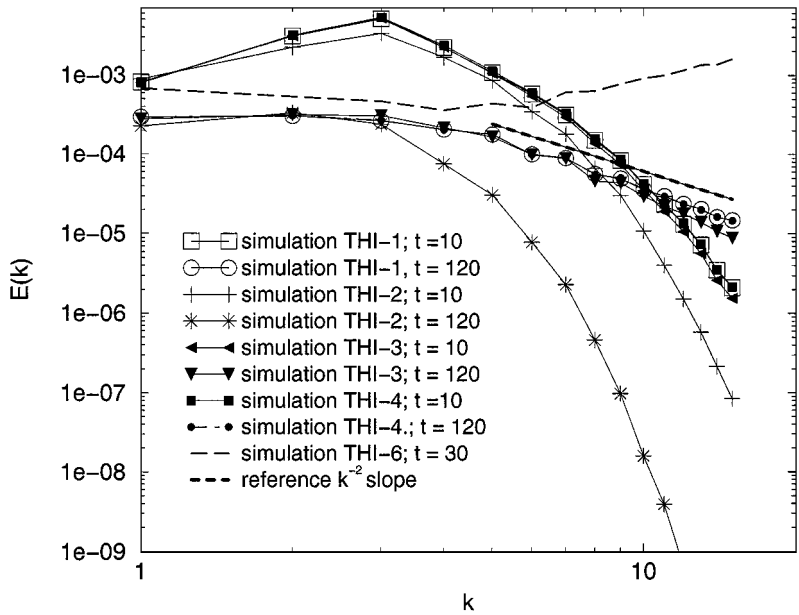

FIG. 1. Kinetic energy spectra for simulations THI-1, THI-2, THI-3, and THI-4, at $t = 10L_{ref}/U_{ref}$ and $t = 120L_{ref}/U_{ref}$. For simulation THI-6, a k^2 spectrum symptomatic of equipartition equilibrium develops.

as shown by the self-similar decay with a constant slope around k^{-2} for the spectra obtained with the FSF model (simulation THI-1) (see Fig. 1). The simulation THI-5 diverges, showing that the skew-symmetric form by itself is not sufficient to sustain such a simulation of compressible turbulence. Notice that, as the skew-symmetric form of the convective term is shown to conserve energy in the incompressible limit (see [45]), such a simulation would be sustained for a truly incompressible regime. The spectrum for simulation THI-6 exhibits a k^2 shape, symptomatic of an equipartition equilibrium [40]: the second order dissipation is able to prevent numerical divergence but not to play a role equivalent to a SGS model. Figures 2 and 3 show the time evolutions over the whole domain of the mean kinetic energy and enstrophy: all simulations with zero fourth-order dissipation exhibit an increase of enstrophy up to a critical time t^*, close to $t \approx 15U_{ref}/L_{ref}$. This time is of the order of the critical time of "enstrophy blow up" (identified as a maximum on Fig. 3) discussed in [40], $t^* \approx 5.9(\frac{1}{2}\omega^2(0))^{-1/2}$, and in [49] for practical LES applications, $t^* \approx 4(\frac{1}{2}\omega^2(0))^{-1/2}$. These evaluations correspond to 28 and $19U_{ref}/L_{ref}$ in our case. The behaviour of energy and enstrophy is anomalous for simulations THI-5 and THI-6, showing the necessity of the LES model.

The first four simulations are continued until $t \approx 10t^*$. For time $t > t^*$, the mean kinetic energy decreases with a $t^{-1.4}$ slope for simulations THI-1 to THI-4, in good agreement with turbulence theories (see [40] for a review): this result is not very sensitive to the the nature of the dissipation. Figure 4 shows the time evolution of the turbulent Mach number, pressure, density, and temperature fluctuations (P_{rms}, ρ_{rms}, T_{rms}) for simulation THI-4. The turbulent Mach number is $M_t \approx 0,13$ for $0 < t < t^*$ and decreases down to $M_t \approx 0.03$ for $t \approx 10t^*$. After some oscillations due to initial conditions, P_{rms}, ρ_{rms}, T_{rms} decrease, showing that an auto-similar state has been reached. The ratio $\int_{\mathcal{V}} (\mathrm{div}\,\mathbf{u})^2\, d\mathcal{V} / \int_{\mathcal{V}} \omega^2\, d\mathcal{V}$ varies from $0 (t = 0)$ to 0.02 for self-similar decay, showing that the turbulence is weakly compressible.

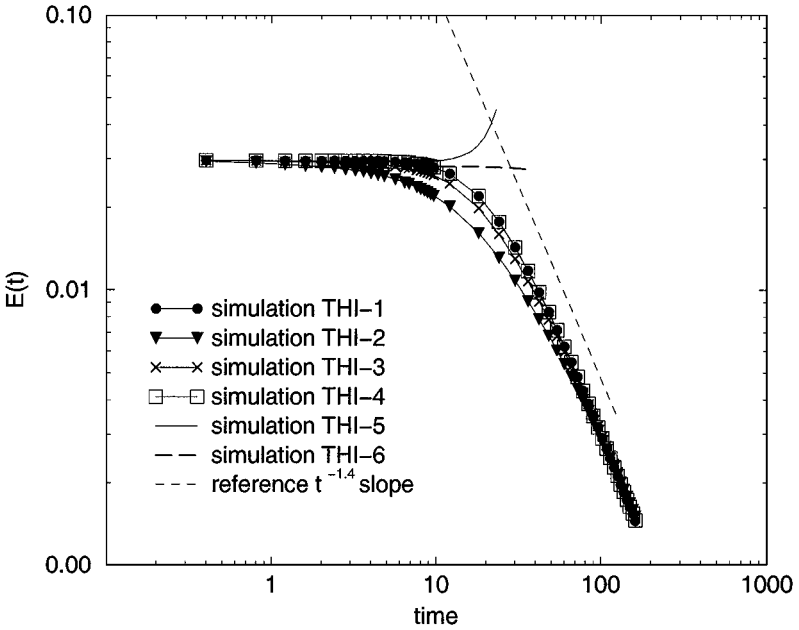

FIG. 2. Time evolution of kinetic energy $\frac{1}{\mathcal{V}}\int_{\mathcal{V}} u^2/2\, d\mathcal{V}$ for simulations THI-1 to THI-6.

The results obtained in simulation THI-1 with the FSF model will now be taken as reference for discussion.

The numerical scheme involving second- and fourth-order dissipation (simulation THI-2) is clearly too dissipative: the kinetic energy level is reduced by more than a decade for scales

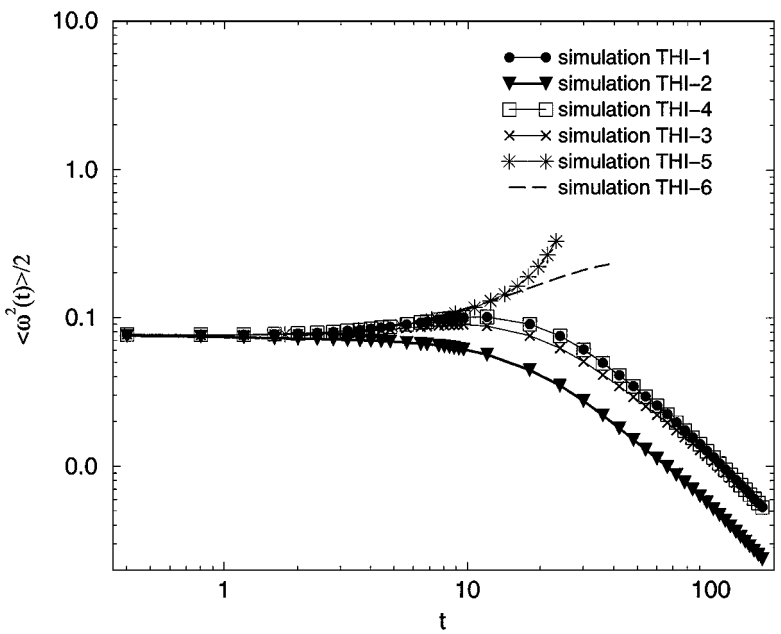

FIG. 3. Time evolution of enstrophy $\frac{1}{\mathcal{V}}\int_{\mathcal{V}} \omega^2\, d\mathcal{V}$ for simulations THI-1 to THI-6.

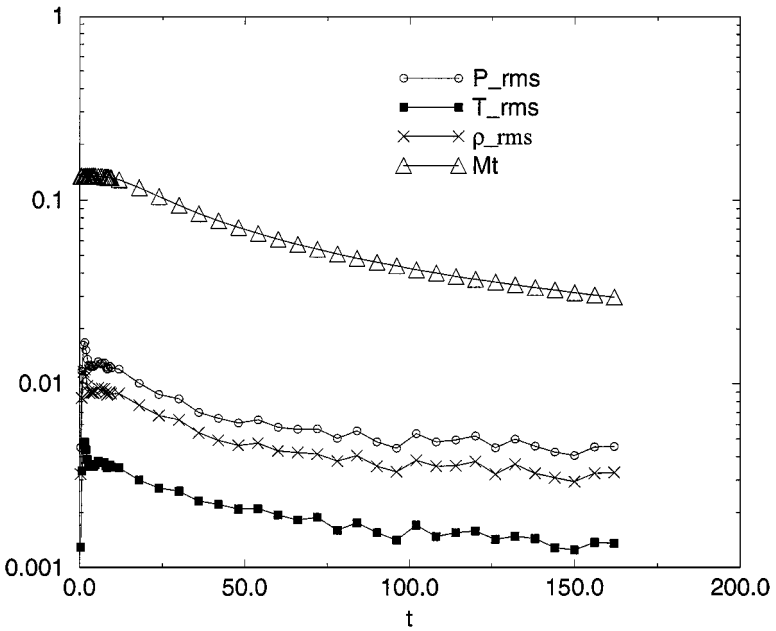

FIG. 4. Time evolution of turbulent Mach number, pressure, temperature, and density fluctuations for simulation THI-4.

of sizes about the cutoff length whereas the large scales are hardly affected (see discussion in Section 5 and Fig. 1). No satisfactory evolution of energy and enstrophy is obtained. A clear improvement of the results is obtained when setting the fourth-order coefficient to zero (simulation THI-3); but even in this case the dissipation brought up by the classical second order Jameson dissipation is large enough to perturb the role played by the subgrid scale model. This is particularly obvious during the early time of evolution when kinetic energy at the cutoff k_c is negligible, and thus where the dissipation brought up by the FSF model is nearly zero.

Although the numerical dissipation (O(2) and O(4)) is sometimes used as a subgrid-scale model (it has indeed the same effects as a dissipative subgrid-scale model on the quantities observed here), it always brings a spurious dissipation, too large when the fourth order is employed and too weak when the second order alone is employed. In consequence, it is not able to mimic the dissipation of a true subgrid-scale model, and therefore is not well adapted to LES. This conclusion is similar to the one provided by Garnier *et al.* [50].

The application of modification (Eq. (22)) corrects these drawbacks and gives the same results as the standard LES for simulation THI-4. Figure 5 shows the time evolution of $\langle\Phi\rangle = \int_{\mathcal{V}} \Phi \, d\mathcal{V}$, $\langle\Psi\rangle = \int_{\mathcal{V}} \Psi \, d\mathcal{V}$, Φ_{rms}, Ψ_{rms} and of the correlation coefficient of Φ and Ψ. Although the mean values and fluctuations of the classical sensor Ψ decrease as expected for a self-similar decay, the mean value and the fluctuations of the correction Φ increase. The global sensor $\Phi\Psi$ is shown to be small, which seems to be not only due to the low values of each component Φ and Ψ, but also due to their relatively weak correlation (see Figs. 5 and 6).

The three remaining simulations concern the Comte-Bellot Corrsin experiment. The initial velocity fields were provided by the Center for Turbulence Research and are described in [24]: they match the CBC experiment condition for $t_0 U_0/M = 42$. The thermodynamic

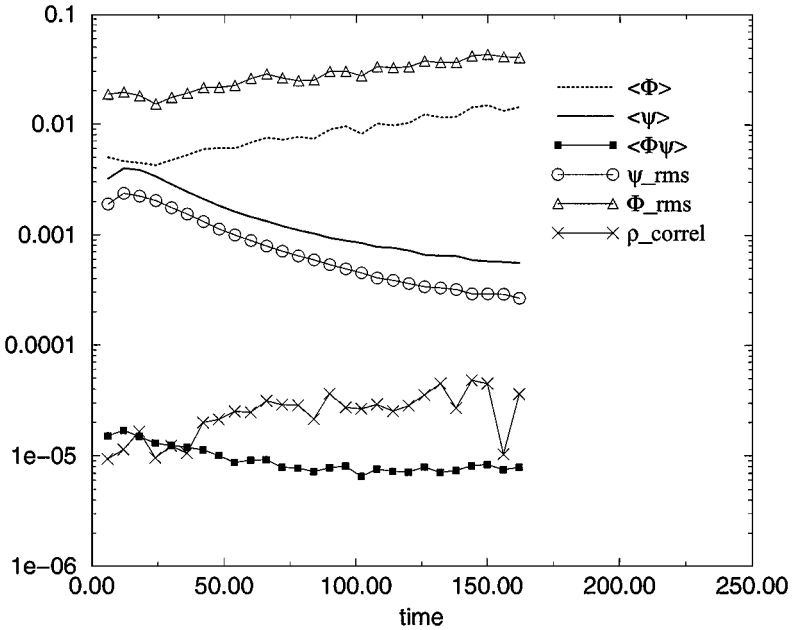

FIG. 5. Time evolution of mean and *rms* values for Φ, Ψ, their product $\Phi\Psi$, and their correlation coefficient for simulation THI-4.

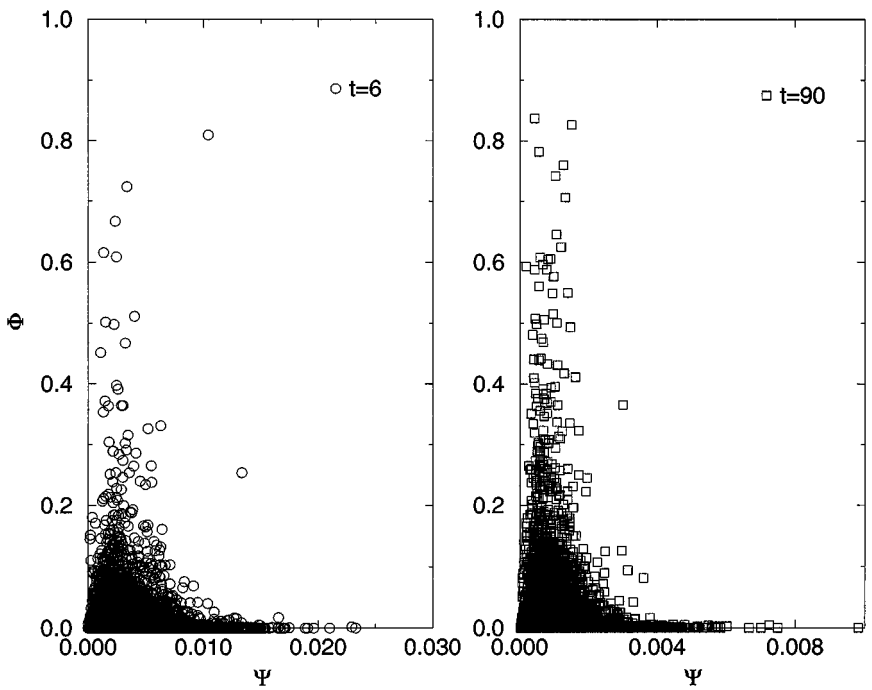

FIG. 6. Scatterings of Φ and Ψ for early ($t = 6U_{ref}/L_{ref}$) and equilibrium stages ($t = 90U_{ref}/L_{ref}$) for simulation THI-4.

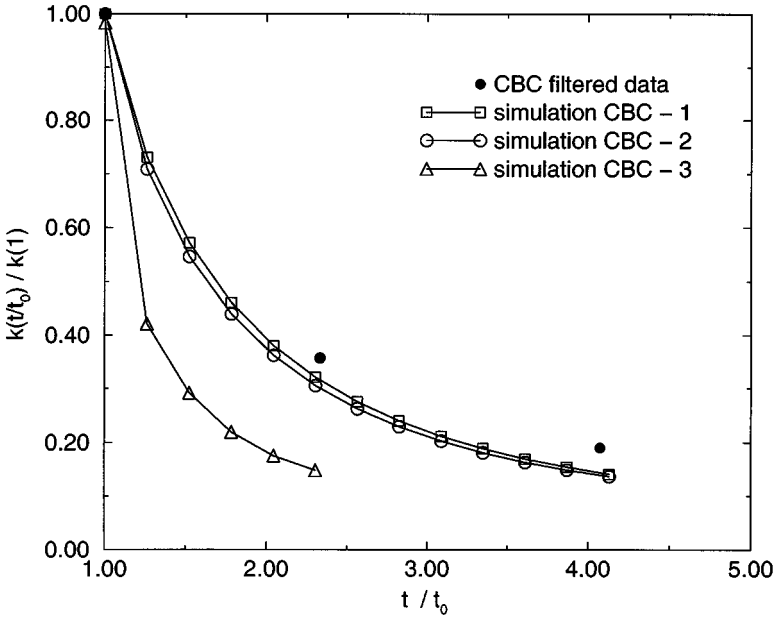

FIG. 7. Time evolution of kinetic energy for simulations CBC-1, CBC-2, and CBC-3, $t_0 = 42M/U_0$.

state is adapted to get M_t to 0.26, which is in the range of the turbulent Mach number considered by Moin *et al.* [24]. Figures 7 and 8 display the time evolution of kinetic energy, normalized by its initial value and the kinetic energy spectra for a time that corresponds to $tU_0/M = 98$, i.e., $t/t_0 = 2.33$. The simulation CBC-1 (see Table I for parameters) provides reasonable results: the error is about 20% on the energy prediction for $t/t_0 = 4.07$,

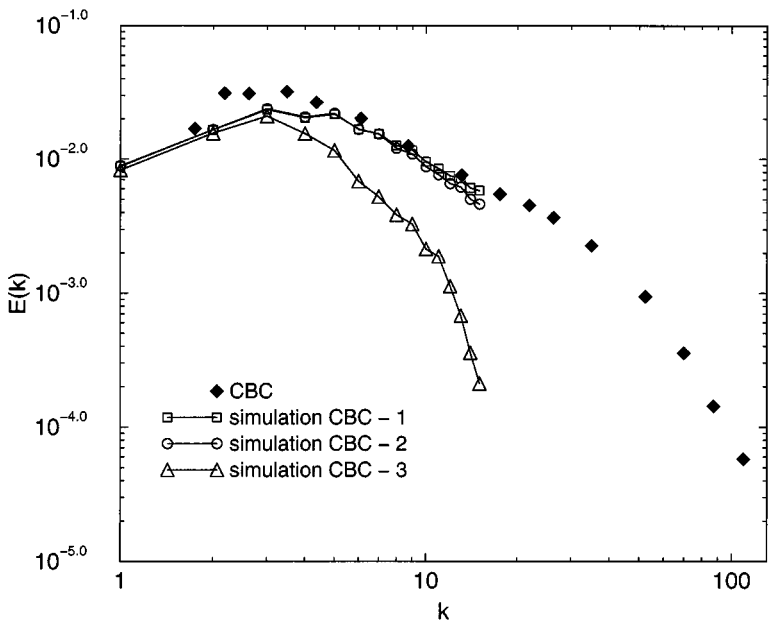

FIG. 8. Kinetic energy spectra for simulations CBC-1, CBC-2, and CBC-3 for $tU_0/M = 98$.

i.e., for the last station of CBC measurements.This result does not seem as good as the ones obtained by Moin *et al.* [24] using the dynamic model, although the dynamic model predicts an equilibrium value of the constant comparable to the value of Smagorinsky constant obtained using isotropic turbulence [24]. Considering the simulation CBC-1 as reference, the simulations CBC-2 and CBC-3 show that the proposed modification is able to maintain similar results (CBC-2) whereas the original Jameson scheme is not (CBC-3). The discrepancy between the CBC-1 and CBC-2 results is larger than between THI-1 and THI-4: this seems due to the higher turbulent Mach number for the CBC cases. Although this could be seen as a limitation of the proposed numerical method, turbulent Mach numbers around 0.25 are already representative of a wide range of applications for aeronautical purposes.

4.2. Two Dimensional Vortex-Shock Interaction

The effect of the proposed correction near a shock is now investigated by simulating the 2D interaction of a vortex and a shock in a configuration described in Fig. 9: the mean flow is in the x-direction; periodic boundary conditions are applied in the y-direction. The purpose of this test case is to compare the numerical results with simple analytical models of vortex amplification through the shock [8]: the main advantages of the 2D configuration being the lack of vortex stretching. The dimensions of the computational domain are $(L_x, L_y) = (4, 1)L_{ref}$; at $t = 0$, a Lamb–Oseen type vortex is centered at $(x, y) = (1, 0.5)L_{ref}$ and is convected by the mean flow (see Lamb [51, p. 592]).

Nine simulations are conducted. For the first six, the upstream Mach number is $M_1 = 1.2$ to match the simulation of Lee *et al.* [7]: this corresponds to an inlet velocity of $U_1 = 1.42U_{ref}$. The maximum tangential velocity is $0.16U_{ref}$, which can stand for a relatively high level of

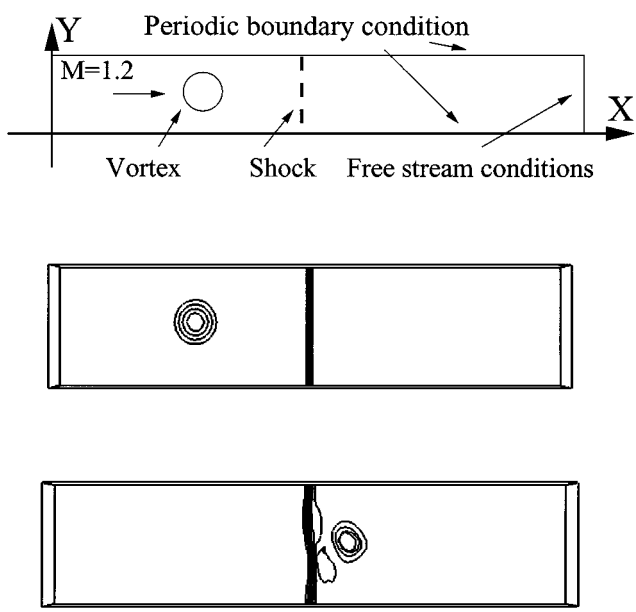

FIG. 9. The 2D shock/turbulence interaction. **Top**, sketch of the simulation; **middle**, initial condition (Lamb–Oseen vortex); iso-lines of vorticity and pressure show the respective positions of the vortex and the shock. **Bottom**, the same lines show the modifications of shape of both vortex and shock contours (see Subsection 4.2).

TABLE II
Parameters of Simulations for the Two Dimensional Vortex/Shock Interaction (See Subsection 4.2)

Simulation	(nx, ny)	k^2	k^4	$\mathcal{N}_y$	Sensor	FSF model
VS-1	128×16	1.5	0.02	8	Ψ	No
VS-2	256×32	1.5	0.02	16	Ψ	No
VS-3	512×64	1.5	0.02	32	Ψ	No
VS-4	128×16	1.5	0	8	$\Phi\Psi$	No
VS-5	256×32	1.5	0	16	$\Phi\Psi$	No
VS-6	512×64	1.5	0	32	$\Phi\Psi$	No

Note. The resolutions are referred to as resolution 1 (respectively 2, 3) for 128×16 (respectively 256×32, 512×64). The fifth column $\mathcal{N}_y$ indicates the number of points in the vortex in the y-direction; twice as many points are used in the x-direction.

equivalent turbulent Mach number. The parameters of these simulations are given in Table II where we use either the classical Jameson's dissipation (second- and fourth-order dissipation) or the modified Jameson one, for three different resolutions: for all simulations, the subgrid scale model is switched off. The number of points involved in the numerical description of the vortex is given for the y-direction: twice as many points are used in the x-direction to resolve the vortex. Three other simulations are conducted using the parameters of simulations VS-6, but with various inlet Mach numbers ($M_1 = 1.1$, 1.4, and 1.7) in order to check the sensitivity to upstream flow.

All simulations (and the ones presented in the next section) are performed in the frame of the shock: the shock, originally placed at $x = L_x/2$, is thus at rest in this frame and its mean position does not change for the present laminar calculation.

Figure 9 displays isolines of pressure and vorticity during the interaction for simulation VS-4. After the shock, the vortex becomes elliptic, which is in agreement with LIA predictions [4] and other numerical results [52].

Figure 10 gives the time evolution of the maximum of $\sqrt{\omega^2(t)/\omega^2(0)}$ on the domain for all simulations of Table II. The expected results are a constant value before the shock-vortex interaction, an increase during the interaction and another constant level when the vortex is in the post-shock region. As stressed in Mahesh *et al.* [8] for incidence angles near zero, this quantity is supposed to scale as

$$\frac{\omega_2}{\omega_1} \approx \frac{\rho_2}{\rho_1} = \frac{U_1}{U_2}, \tag{25}$$

ω_2 (respectively ω_1) standing for post- (respectively pre-) shock position of the vortex. Additional tests at higher Mach numbers using the modified sensor are presented in Fig. 11. Expected results are qualitatively and quantitatively recovered in all cases. However, two phenomena are worth noting.

The first concerns pre- and post-shock regions, where only the fourth-order dissipation of the classical Jameson's dissipation is supposed to act. A decrease of enstrophy is observed in the pre-shock and/or post-shock regions for the simulations VS-1 and VS-2, showing the influence of the fourth-order dissipation as in the previous section. Simulations VS-3 and VS-6 show that well resolved scales are not affected by the fourth-order dissipation. Moreover, the distortion of the vortex in post-shock regions makes the pressure gradient steeper and enables the sensor of the classical second-order Jameson's dissipation to bring a

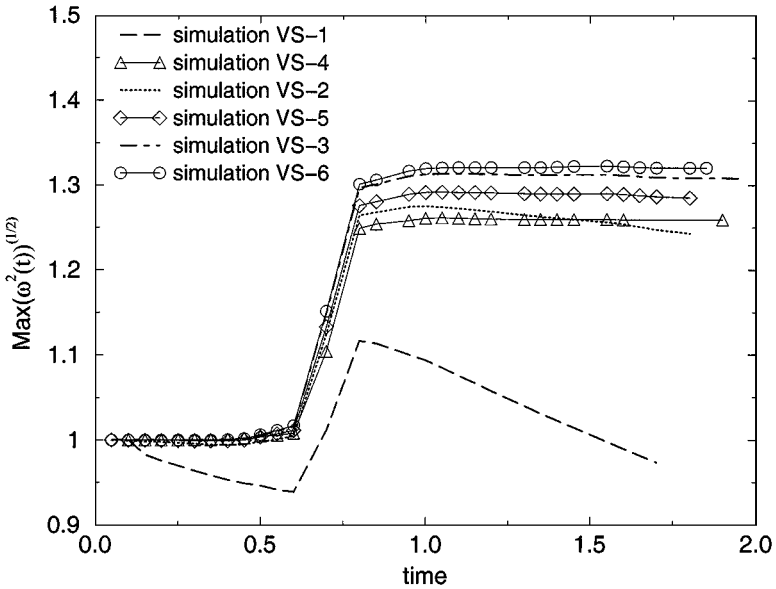

FIG. 10. Time evolution of the maximum of $\sqrt{\omega^2(t)/\omega^2(0)}$ for the 2D shock/vortex interaction; long dashed line, simulation VS-1; doted line, simulation VS-2; dot-dashed line, simulation VS-3; △, simulation VS-4; ♢, simulation VS-5; ◯, simulation VS-6.

larger dissipation than for the pre-shock region (simulation VS-2). For all cases, the proposed correction maintains a plateau for enstrophy in both the pre- and post-shock regions.

Second, the enstrophy growth through the shock is captured more precisely with increasing resolution and for a fixed resolution when applying the $\Phi\Psi$ sensor. As previously

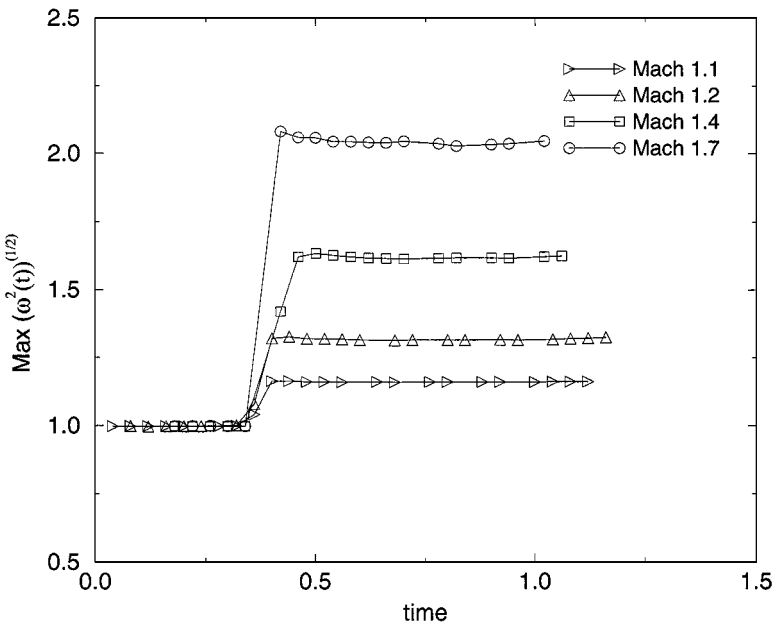

FIG. 11. Time evolution of the maximum of $\sqrt{\omega^2(t)/\omega^2(0)}$ for parameters of simulation VS-6 for $M_1 = 1.1$, 1.2, 1.4, 1.7. The curves have been displaced so that the dates of the shock/vortex interaction coincide for all Mach numbers.

underlined, an increased number of points results in steeper gradients and thus a larger production of enstrophy; this fact is already investigated in [7]. The sensor $\Phi\Psi$ increases this trend. Simulations confirm these conclusions for Mach numbers ranging from 1.1 to 1.7.

4.3. The 3D Shock-Turbulence Interaction

4.3.1. *Parameters*

The previous schemes are now tested in the case of the interaction between a weak compressible turbulence and a shock. The mean flow is in the x-direction; periodic boundary conditions are applied in the y- and z-directions. The configuration of the simulation is described in Fig. 12 and is similar to the one treated in [7] except for the fact that the incident turbulence is not prescribed at the inlet through an adapted procedure for which the spectrum is given [53] but through the direct input of LES fields obtained in Subsection 4.1 and the use of Taylor's hypothesis: the same choice has been made by [8]. An extensive study of the validity of Taylor's hypothesis for compressible flow is proposed in [53]. This hypothesis is shown to be valid for the case treated here since the inlet turbulent Mach number M_t is about 0.075 and the inlet turbulence intensity is low ($\sqrt{q}/U_1 \approx 0.06$). The dimensions of the calculation domain are $(L_x, L_y, L_z) = (2, 1, 1)L_{ref}$. The smallest resolved kinetic energy scale of the incident turbulence is thus $L_{uvw} = L_{ref}/16$ (see Section 2). The resolution is $(ny, nz) = (32, 32)$ points in both the y- and z-directions to match the resolution of the previous isotropic turbulence simulation. Three resolutions are used in the x direction: the first is 64 points (which gives an isotropic grid $dx = dy = dz = L_{ref}/32$; it is referred to as resolution 1, used for simulations ST-1 and ST-2). For simulations ST-3, 4, 5, the x discretization is equivalent to the previous one for the inlet, then smoothly refined up to $dx(i) \approx 1/8(L_{ref}/32)$ just before the shock and for the rest of the domain (simulations ST-3, 4), or only in a region around the shock (simulation ST-5). For the chosen grid refinement, the ratio between the integral scale of the incoming turbulence and the mesh size in the shock region is about half of the ratio between the vortex and the width of the mesh for the resolution 3 of the previous 2D cases (see Fig. 13). This suggests that the mesh for cases ST-3, 4, 5 is sufficient to describe properly the interaction of the more energetic structures

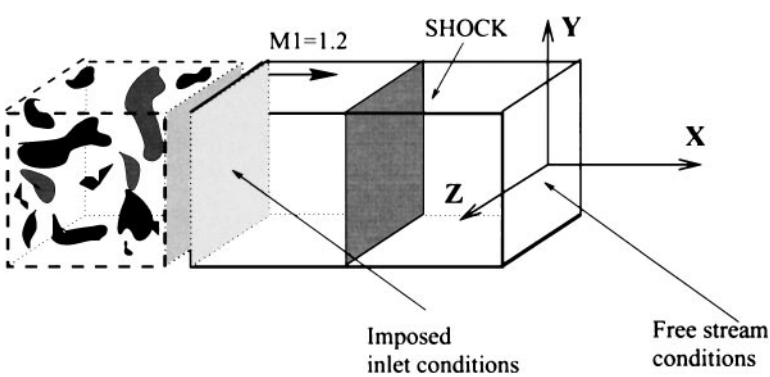

FIG. 12. Schematic diagram of the computational domain for simulations ST-1 to ST-5. Periodic conditions are applied in the y- and z-directions (see Subsection 4.3).

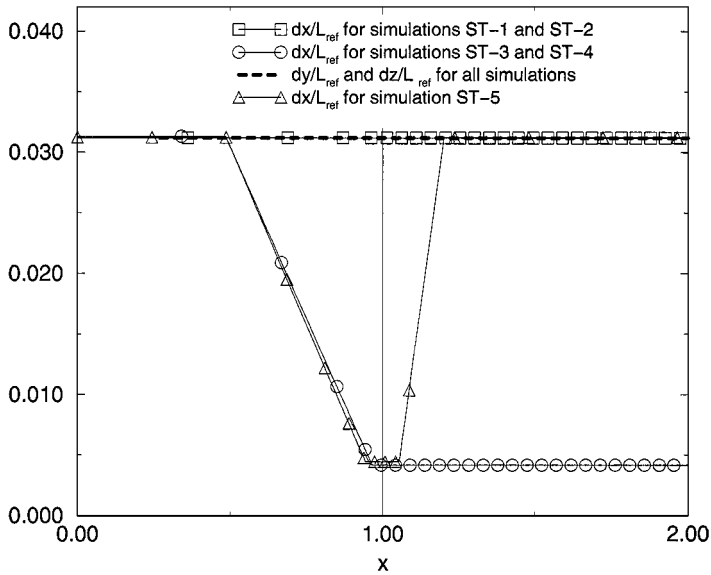

FIG. 13. x distribution of the cell sizes dx, dy, and dz in the x-, y-, and z-directions for simulations ST-1, 2, 3, 4, 5. A dashed line marks dy and dz for all simulations; □, dx for resolution 1 (simulations ST-1 and ST-2), ◯, dx for resolution 2 (simulations ST-3 and ST-4), △, dx for resolution 3 (simulation ST-5). The vertical line denotes the initial shock position.

with the shock, at least with the same accuracy as for the shock/vortex interaction previously treated. This refinement is close to the solution used by [54] to recover DNS results with a shock capturing technique. The parameters are summarized in Table III: for all simulations, the FSF model is switched on. The problems of LES formulation on variable meshes were neglected in the present work, which seems reasonable regarding the global order of our numerical method and the low stretching of the mesh [55]. However, independently of the problem of commutativity between filter and space derivatives, the strong change of cutoff length in the x direction will have a crucial effect on the dynamic on vorticity dynamics (see below).

The procedure to obtain statistics was inspired by the work of [53] and has been adapted to LES fields, for which we forget the notation devoted to resolved motion: f stands now

TABLE III
Parameters of Simulations for the Three Dimensional Shock/Turbulence Interaction (See Subsection 4.3)

Simulation	(nx, ny, nz)	Grid	k^2	k^4	Sensor	FSF model
ST-1	$64 \times 32 \times 32$	Isotropic	1.5	0.02	Ψ	Yes
ST-2	$64 \times 32 \times 32$	Isotropic	1.5	0	$\Phi\Psi$	Yes
ST-3	$262 \times 32 \times 32$	Locally refined	1.5	0.02	Ψ	Yes
ST-4	$262 \times 32 \times 32$	Locally refined	1.5	0	$\Phi\Psi$	Yes
ST-5	$156 \times 32 \times 32$	Locally refined	1.5	0	$\Phi\Psi$	Yes

Note. The resolutions are referred to as resolution 1 (respectively 2, 3) for $64 \times 32 \times 32$ (respectively $262 \times 32 \times 32$ and $156 \times 32 \times 32$).

for $\tilde{f}$ or $\bar{}$ and $\tilde{}$ being reserved for spatial and time averages:

$$\bar{f}(x) = \int_{Ly}\int_{Lz}\int_{T} f(x,y,z,t)\,dt\,dz\,dy, \qquad \tilde{f}(x) = \frac{\overline{\rho(x,y,z,t)\,f(x,y,z,t)}}{\overline{\rho(x,y,z,t)}} \tag{26}$$

and

$$f'(x,y,z,t) = f(x,y,z,t) - \bar{f}(x), \qquad f''(x,y,z,t) = f(x,y,z,t) - \tilde{f}(x). \tag{27}$$

Mean streamwise fluctuations are then defined in a logical manner $\bar{f}'(x)$, $\bar{f}''(x)$, etc. Once a stationary state is reached, time sampling is performed over $12L_{ref}/U_{ref}$ for simulations ST-1, ST-2, and ST-5 and over $5L_{ref}/U_{ref}$ for simulations ST-3 and ST-4.

4.3.2. *Mean Flow Variables*

Figures 14 and 15 show the distribution of the mean streamwise velocity, pressure, and Mach number through the shock. As noticed in [56], mean variables obey modified Rankine–Hugoniot jump conditions. The downstream values of the variables obtained in the turbulent case undergo slight over- or undershoots depending on the variables downstream to the shock before relaxing to the laminar values. This fact is more pronounced for resolution 2 where the reduced grid spacing allows a more accurate description of the thermodynamic fluctuations and the rise of steeper gradients: this fact will be discussed below.

4.3.3. *Turbulent Kinetic Energy, Mach Number, and Reynolds Stresses*

Let us define the Reynolds stress tensor by

$$R_{ij}(x,y,z,t) = \widetilde{u_i'' u_j''} = \frac{\overline{\rho u_i'' u_j''}}{\bar{\rho}}. \tag{28}$$

The turbulence kinetic energy is then defined by $E(x,y,z,t) = (1/2)(R_{11} + R_{22} + R_{33})$, its mean streamwise value by $\bar{E}(x)$. Figures 16 and 17 show the evolution of the normalized turbulence kinetic energy and of the turbulent Mach number for some simulations of Table III. As expected from the previous results obtained in freely decaying turbulence, only the modified $\Phi\Psi$ sensor is able to predict a correct decay of turbulence kinetic energy for the pre-shock region, and this independently of the resolution in the x-direction. The streamwise decrease of kinetic energy is compatible with the one found for homogeneous turbulence when using Taylor's hypothesis (simulations ST-2 and ST-4). The standard Jameson's artificial viscosity exhibits a spurious dissipation (simulations ST-1 and ST-3). The production of $\bar{E}(x)$ is larger in both the shock and the post-shock regions for resolution 2 than for resolution 1.

The evolution of the turbulent Mach number exhibits the same trends: M_t decreases from $M_t \approx 0.075$ at the inlet to M_t between 0.061 (simulations ST-1 and ST-3) and 0.068 (simulations ST-2 and ST-4) just before the shock.

As observed in previous studies (see [6, 7, 13]), the isotropic flow becomes axisymmetric through the shock. This is shown by the streamwise distribution of the Reynolds stresses $\widetilde{R_{ii}}(x)$, obtained with the modified Jameson's sensor (simulations ST-2 and ST-4,

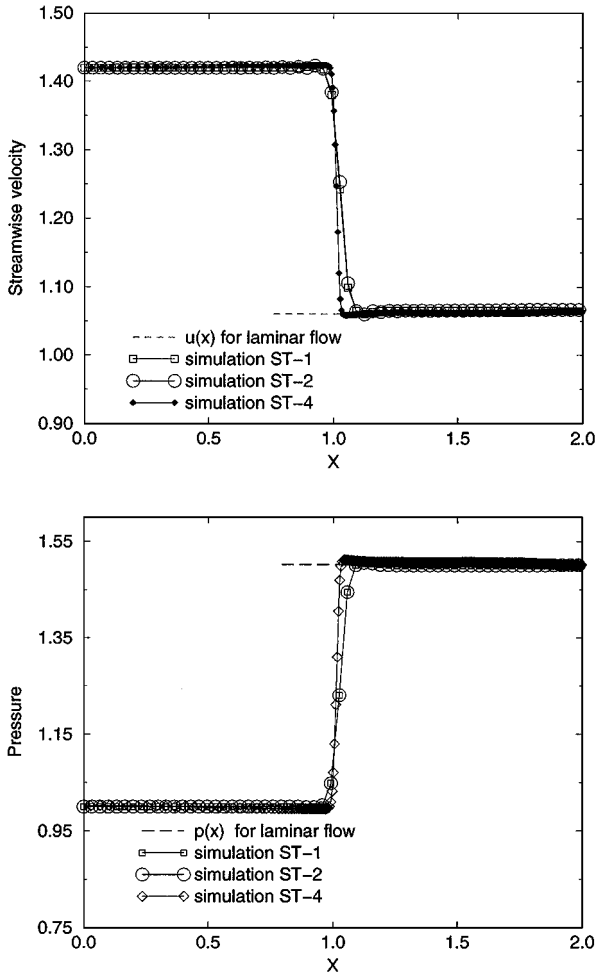

FIG. 14. x distribution of mean steamwise velocity $\tilde{u}$ (top) and mean pressure $\bar{p}$ (bottom) across the shock wave for simulations ST-1, ST-2, and ST-4; dashed lines denote the laminar values satisfying Rankine–Hugoniot jump conditions; □, simulation ST-1; ◯, simulation ST-2; ♢, simulation ST-4.

see Fig. 18): these results compare well with previously mentioned works. A quantitative comparison for the intensity of the Reynolds stresses in the far field is proposed in Table IV: LIA results are estimated from Lee *et al.* [54]. The present results cover the increase of Reynolds stresses arising between the pre-shock region and $x \approx 1.4$ (distant from

TABLE IV
Reynolds Stresses Growth through the Shock

	Lee's (93)	LIA	ST-2	ST-4	ST-5
A	19%	34%	25%	37%	41%
B	4.4%	10%	0%	6%	6%

Note. $A = R_{11}(\textit{post-shock})/R_{11}(\textit{pre-shock})$, $B = R_{22}(\textit{post-shock})/R_{22}(\textit{pre-shock})$. Results of Lee *et al.* are estimated from Fig. 5 of [7]; LIA predictions are estimated from Fig. 4 of [7] for far field.

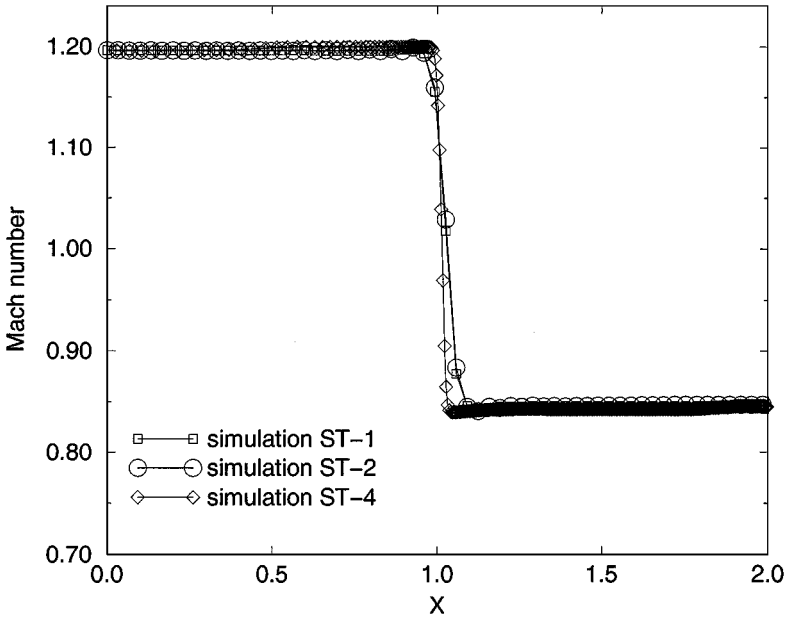

FIG. 15. The x distribution of mean Mach number for simulations ST-1, ST-2, and ST-4 with the same legend as the previous figure.

the shock from approximatively one integral length-scale of the incident turbulence). Although LIA predictions are to be considered with care since the composition of the incident turbulence is able to influence the results [8], presented results (for ST-4 and ST-5) agree well with previous ones, ST-2 results being clearly of lower quality. Lower predictions obtained using DNS may be due to viscosity effects; such effects have been reported by Lee *et al.* [6].

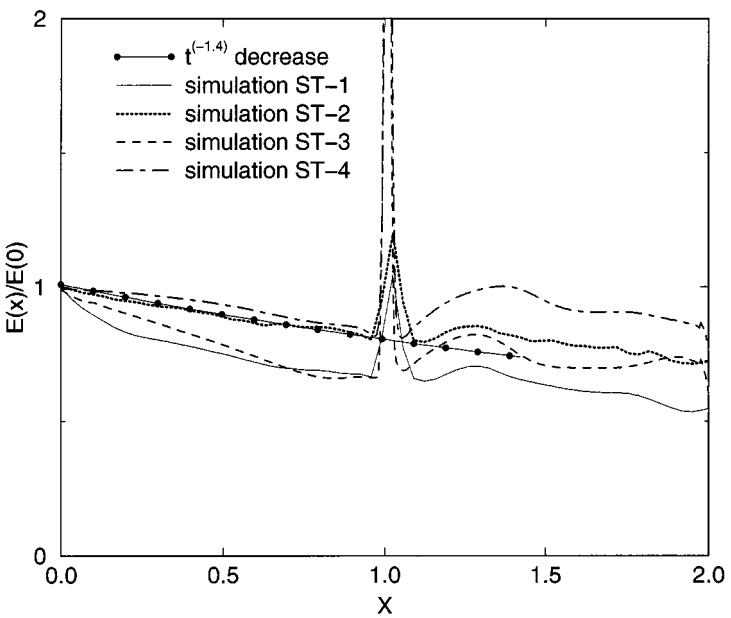

FIG. 16. The x distribution of normalized turbulence kinetic energy $\overline{E(x)}/\overline{E(0)}$ for stimulations ST-1–4.

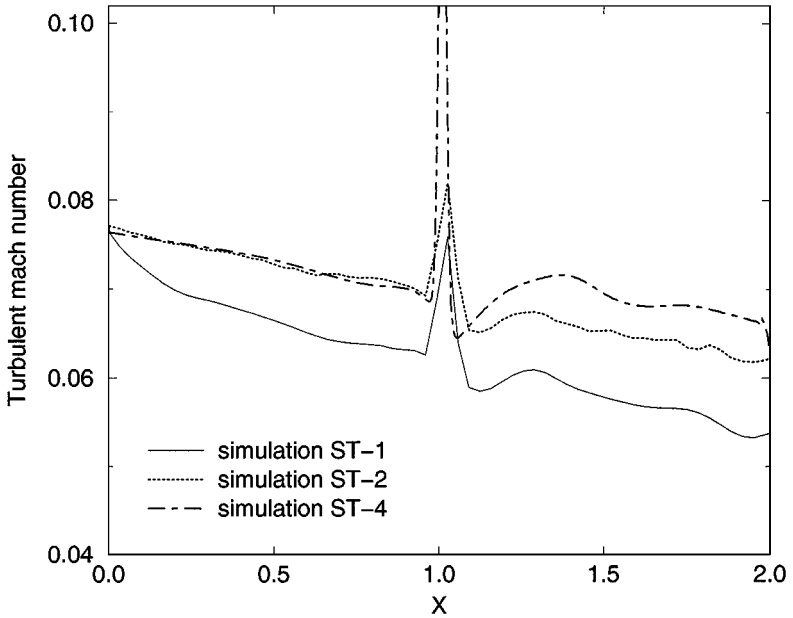

FIG. 17. The x distribution of turbulent Mach number $\bar{M}_t$ for simulations ST–1, 2, 4.

Lee *et al.* [7] investigate the budget of the mean kinetic energy equation and show that the pressure work and the viscous terms are the main contributors to the evolution of kinetic energy outside the shock wave: as the Reynolds number is set to infinity, only the subgrid-scale modeling and the artificial dissipation can contribute to dissipation. The larger increase obtained with the $\Phi\Psi$ sensor and the refined mesh (simulations ST-4 and

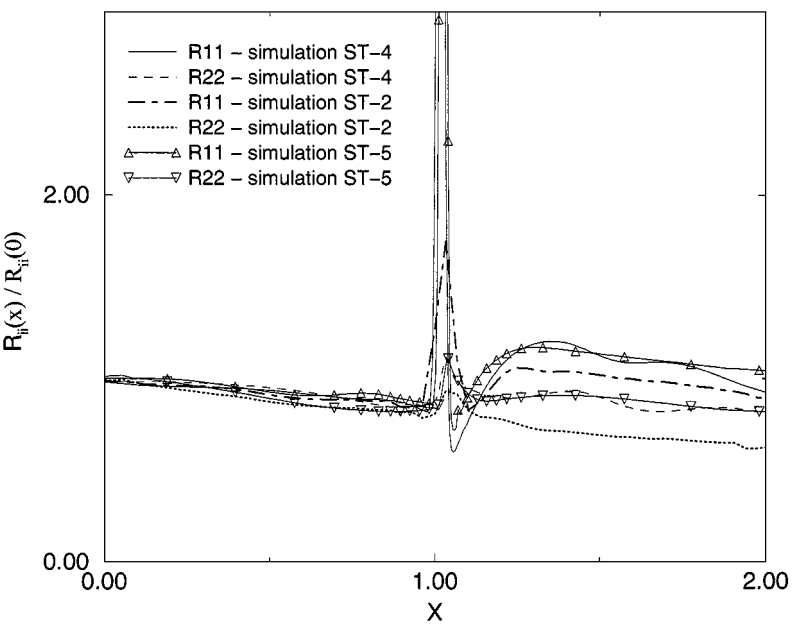

FIG. 18. The x distribution of normalized Reynolds stresses $\tilde{R}_{ii}(x)/\tilde{R}_{ii}(0)$ for stimulations ST-2, 4, 5.

ST-5) confirms the weak dissipative properties of the present numerical method used in combination with grid refinement. Indeed the same numerical method used without grid refinement exhibits a weaker increase of Reynolds stresses behind the shock and leads to a non-physical behaviour: R_{22} peaks before the minimum value of R_{11} both in the results of [7] and in the present results obtained with the refined mesh (simulations ST-4, 5). This is no longer true using the coarse grid (see Fig. 18, simulation ST-2). The present results confirm that grid refinement leads to a proper description of pressure work and a limited dissipation.

4.3.4. *Vorticity*

Figures 19 and 20 display the streamwise distribution of normalized vorticity fluctuations $\overline{\omega_x'^2}(x)/\overline{\omega_x'^2}(0)$ and $\overline{\omega_z'^2}(x)/\overline{\omega_z'^2}(0)$. As already mentioned, the standard sensor used to trigger Jameson's dissipation predicts a spurious decay of vorticity, even before the shock region. This non-physical behaviour is corrected by means of the $\Phi\Psi$ sensor. Although previous studies (LIA and DNS results) suggest that the streamwise component $\overline{\omega_x'^2}$ is hardly affected across the shock, this tendency is recovered only for simulations ST-1, 3, 4, 5 and not for ST-2: the use of modified Jameson's dissipation together with a non-refined mesh exhibits a decrease of $\overline{\omega_x'^2}$ through the shock. The amplification of the transverse component $\overline{\omega_z'^2}$ is predicted with different intensities for all simulations (85% for ST-4, 80% for ST-5, from 60 to 80% depending on the incident turbulent Reynolds numbers for [6], and around 80% for LIA prediction extrapolated from Fig. 8 of [6]). This is compatible with the results of Lee *et al.* [6]. Although the dynamic of enstrophy does not follow the same rules for 3D cases as in 2D cases, it may be underlined that the registered vorticity increase approximately scales on the density ratio for this low Mach number case. In the present LES, coarse grid results suggest that no grid refinement leads to a monotonic decay of both transverse and

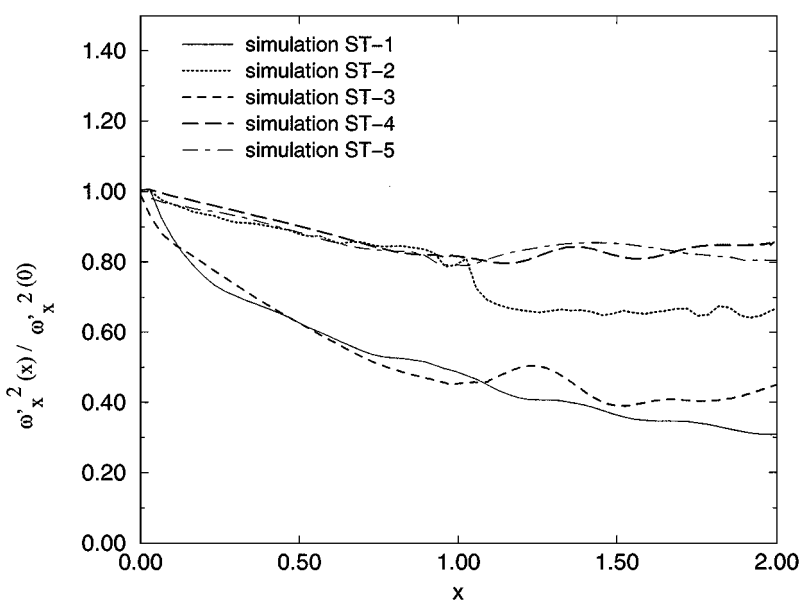

FIG. 19. The x distribution of normalized fluctuations vorticity component $\overline{\omega_x'^2}(x)/\overline{\omega_x'^2}(0)$ for simulations ST-1–5.

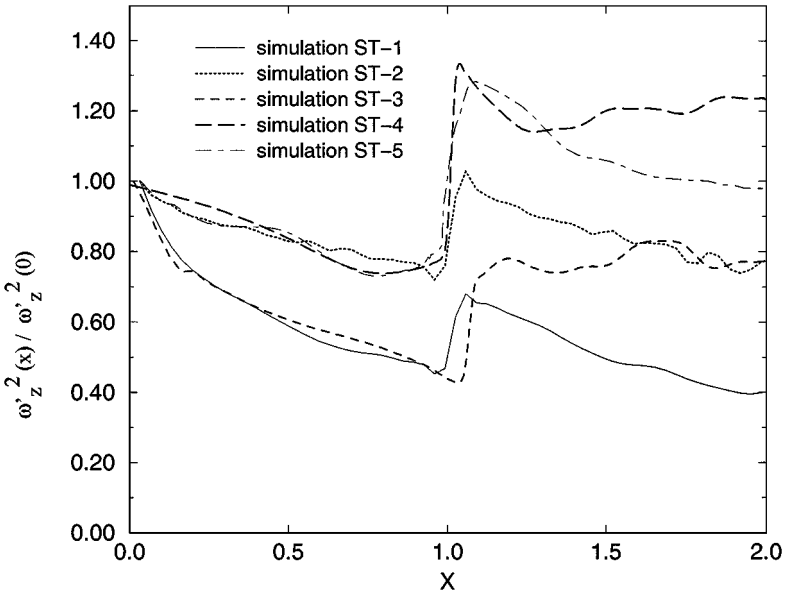

FIG. 20. The x distribution of normalized fluctuations vorticity component $\overline{\omega_z^2}(x)/\overline{\omega_z^2}(0)$ for simulations ST-1–5.

streamwise components and to erroneous results through the shock. The simulation ST-5 is able to produce correct results through the shock together with a more or less monotonic decay of vorticity components. This is no longer the case for the resolution 2 (simulations ST- 3 and ST-4), for which both streamwise and transverse components of vorticity increase. Although the method used to refine the grid around the shock region is not unique and may change the result, this suggests that the convection of very high Reynolds number (in fact infinite) turbulence from an isotropic to an anisotropic more refined grid is responsible for the enstrophy increase far from the shock. This allows energy to cascade from the cutoff wavenumber $k_{c1} \approx 32/L_{ref}$ to $k_{c2} \approx 8 * 32/L_{ref}$ and induces an increase of enstrophy, which is not connected with the present shock interaction problem but is related to turbulence dynamics (see Subsection 4.1). This phenomenon seems more intense for the y and z components as the mesh refinement is acting directly on them (through $\partial/\partial x$), whereas little effect is seen for the x component ($\partial/\partial y$ and $\partial/\partial z$ are unchanged even in the refined meshes.)

4.4. A Posteriori Test on the Modified Sensor

Figures 21 and 22 show the streamwise evolution of the components of the correction (Φ, Eq. (22)) applied to the standard Jameson sensor Ψ. The analysis deals with the fields obtained from simulations ST-2 and ST-4. The hypothesis of weakly compressible turbulence is clearly supported by the low level of dilatation compared to enstrophy. As mentioned, the level of enstrophy in the post-shock region is larger for resolution 2 (simulation ST-4). The width of the region covered by the non-zero dilatation field is to be connected with the instantaneous corrugation of the shock and with the slow drift of the mean shock position [6]. Moreover, the larger prediction of the dilatation for resolution 2 may be due to a steeper shock.

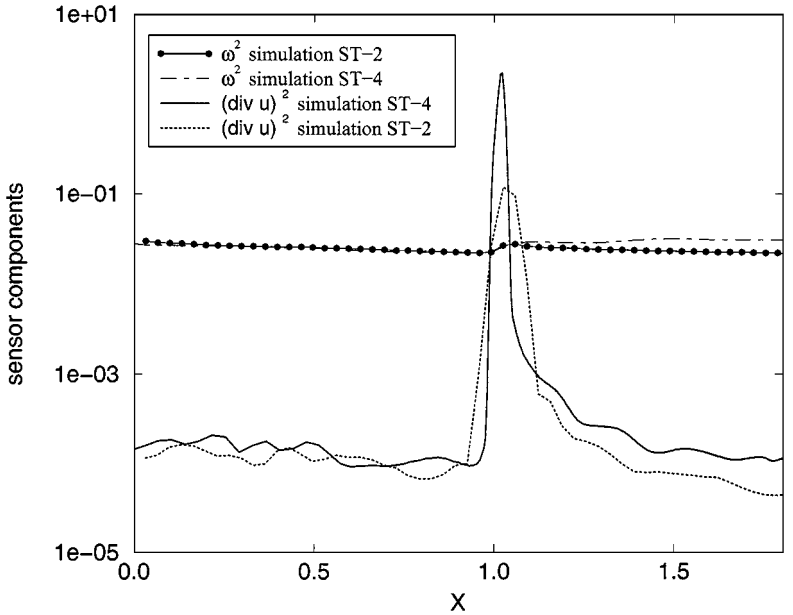

FIG. 21. The x distribution of the components $\overline{\omega^2}(x)$ and $(\mathrm{div}\,\mathbf{u})^2(x)$ of the correction Φ applied to the Jameson's standard sensor Ψ for simulations ST-2 and ST-4 (log-linear plot).

Figure 23 provides three isosurfaces of the instantaneous correction Φ obtained for the simulation ST-2. The lowest level chosen for Φ selects small scales and theoretically allows some dissipation: however, the weak level of correlation between Φ and Ψ away from shock regions (see Subsection 4.1) leads to low values of $\Phi\Psi$ and strongly limits second-order

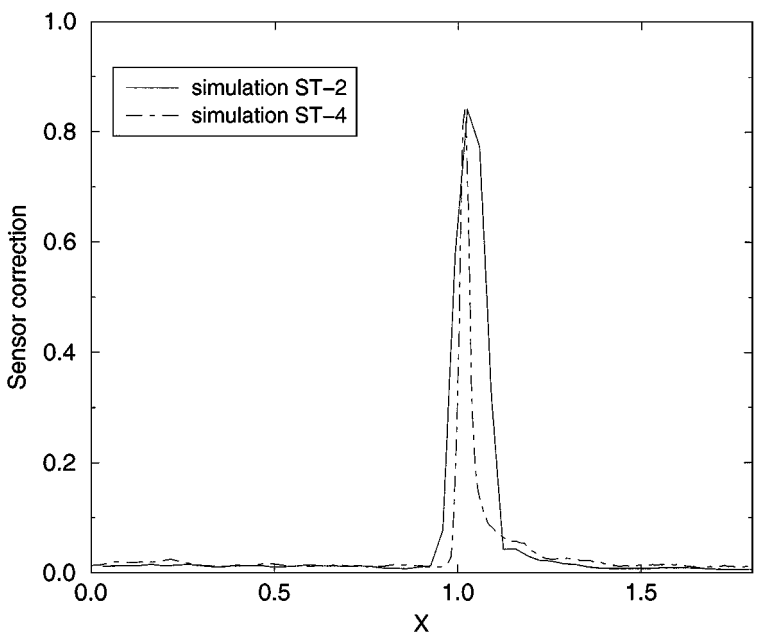

FIG. 22. The x distribution of the correction $\overline{\Phi}(x)$ applied to the Jameson's standard sensor for simulations ST-2 and ST-4.

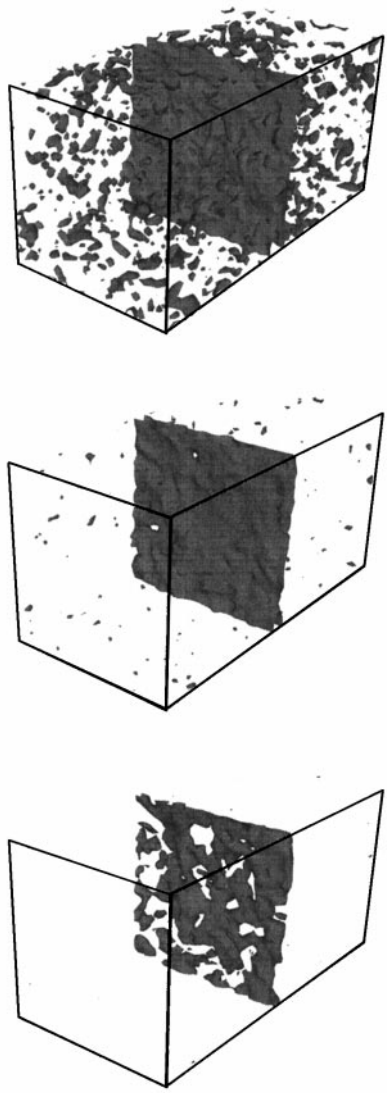

FIG. 23. Instantaneous isosurfaces of Φ taken for simulation ST-2. $\Phi = 0.1$ (top), $\Phi = 0.5$ (medium), and $\Phi = 0.8$ (bottom). The mean flow goes from front to the rear.

dissipation. The selection of higher values ($\Phi = 0.5$ and $\Phi = 0.8$) shows the ability of the sensor to select the shock region and even to reduce the standard Jameson sensor value (there are some holes in the isosurface $\Phi = 0.8$).

Figure 24 compares the standard subgrid scale dissipation acting on kinetic energy ($\epsilon_{sgs} = -\tau_{ij}\tilde{S}_{ij}$) to the second-order dissipation with and without correction Φ. The fourth-order dissipation has not been used here. The whole domain can be split into two parts: the first one is the non-shocked regions where ϵ_{sgs} dominates but where the dissipation coming from the standard second-order can be non-negligible (around 10%). The proposed correction is able to get rid of this problem and sets the second-order dissipation contribution to a negligible level in such regions. These conclusions hold for regions where the grid is refined. The second part consists of the shocked region where ϵ_{sgs} is dominated by the

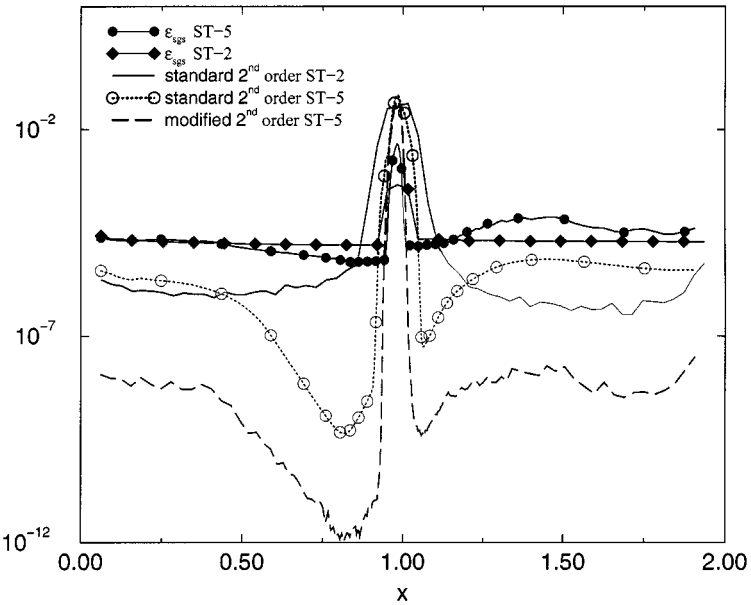

FIG. 24. The x distribution of kinetic energy dissipation coming from both subgrid scale modeling ϵ_{sgs} and artificial viscosity with and without modified sensor (taken from simulations ST-2 and ST-5).

numerical dissipation, leading to a weak influence of the subgrid scale modeling in such regions, at least for the numerical scheme used here.

5. DISCUSSION

The previous results can be used to explain the role of the different dissipations involved in these simulations.

1. Fourth-order dissipation. In the region out of the shock, the only dissipation is provided either by the subgrid scale model ν_t, or by the second and/or the fourth-order term of Jameson's dissipation, depending on the use of the correction (22). Assuming that the dissipative operators take the same form for compressible and incompressible flows, we now consider an equivalent incompressible flow, for which the equation of conservation of kinetic energy in spectral space reads, for the present numerical method,

$$\left(\frac{\partial}{\partial t} + 2\nu_t k^2 + 2\epsilon^{(2)}k^2 + 2\epsilon^{(4)}\frac{k^4}{k_c^2}\right)\bar{E}(k,t) = T^{k<k_c}(k,t). \tag{29}$$

$T^{k\langle k_c}(k,t)$ stands for the triple-velocity correlation coming from resolved non-linear interactions (see [40], for example). A more adapted equation for kinetic energy in spectral space can be found in [30] for compressible flows but it leads to the same discussion. The dissipation acts like $\nu_t k^2 E(k,t)$, $\epsilon^{(2)}k^2E(k,t)$, and $\epsilon^{(4)}k^4E(k,t)$, which explains why the use of the fourth-order dissipation is so crucial for small scales damping and can rapidly lead to an over-dissipative behaviour when the coefficient is a priori fixed as it is the case for Jameson's artificial dissipation. An interpretation of high-order dissipative operators in terms of subgrid scale modeling is proposed by [39] within the formulation in physical space of a spectral eddy viscosity accounting for a cusp behaviour near k_c.

2. Standard Jameson's dissipation. The use of an arbitrary dissipative numerical method (the standard Jameson's artificial viscosity for the present study) can lead to a fairly good picture of the flow (increase of energy, of transverse vorticity fluctuations and continuity of streamwise vorticity fluctuations through the shock). But this picture is not correct far from the shock where the large artificial dissipation affects turbulence more than the subgrid scale model, leading to a wrong prediction of kinetic energy dissipation, as shown by simulation ST-1 and as confirmed by a priori testing.

3. Modified Jameson's dissipation on uniform mesh. The use of the sensor $\Phi\Psi$ to recover a reliable prediction of kinetic energy decay of turbulence out of the shock leads to better results but may encounter some anomalous reduction of the streamwise vorticity component through the shock (see Fig. 19).

This may be explained by the numerical treatment of the different scales involved in this flow: the relevant physical scales are the turbulent scales and the scale λ that characterizes the width of the shock. Turbulent scales extend from large scales (size about $L_{ref}/3$ for all simulations) to the smallest resolved ones of size $Ł_{uvw}(\mathbf{x})$ (see Section 2). In the shock region, the dominant dissipation is provided by the second-order term of Jameson's dissipation, which enables us to capture the shock within typically three points, leading to $\lambda \approx \Delta_c$ for simulations ST-1 and ST-2. Consequently, for all simulations allowing the smallest resolved energetic scales L_{uvw} of size about Δ_c to reach the shock region, the second-order dissipation acting on scales of size λ will affect the flow: this leads to lower increase of kinetic energy, R_{ii}, $\overline{\omega_z'^2}$ components and to a reduction of the streamwise vorticity component through the shock. This is the case for the simulation ST-2, for which $L_{uvw} \sim \lambda \approx \Delta_c \approx L_{ref}/16$.

The other simulations (ST-1, 3, 4, 5) do not allow this to happen because the size of the smallest incident turbulent structures is larger than the width of the shock for all of them.

For simulation ST-1, the use of a standard Jameson's dissipation induces a strong non-physical reduction of the kinetic energy at small scales before reaching the shock region. We have seen that the reduction of the kinetic energy for the scales of size about Δ_c is more than a decade when compared to simulations performed with the modified sensor (see Subsection 4.1). Consequently, the second-order dissipation acts slightly on small resolved energetic scales in the pre-shock region. Figure 25 displays a cut of instantaneous streamwise and transverse components of vorticity for simulation ST-1: nearly no change in size and intensity of the scales is visible for the two components. The size of the smallest scales is clearly larger than the width of the shock. This simulation contains only weakly energetic small scales near the cutoff length scale Δ_c.

4. Modified Jameson's dissipation on refined mesh. Figure 26 displays the same variables as Fig. 25 for simulation ST-4: only a little change of intensity can be seen for the ω_x component whereas the intensity of ω_z increases through the shock and some structures of smaller scales appear in the post-shock region.

Simulation ST-4 benefits from a grid refinement that allows a "numerical" separation between the smallest resolved scales of the turbulent motion ($Ł_{uvw} \approx L_{ref}/16$) and the width of the local shock ($\lambda \approx 3dx(\mathbf{x}) \approx 3/(8*32)L_{ref}$). This leads first to limited damping of the smallest scales through the shock and second to a larger increase of vorticity, due to the occurrence of steeper gradients.

A final important point may be made when discussing the solution adopted for simulations ST-4, 5. Indeed, the previous separation of scale is clearly due to the fact that the grid

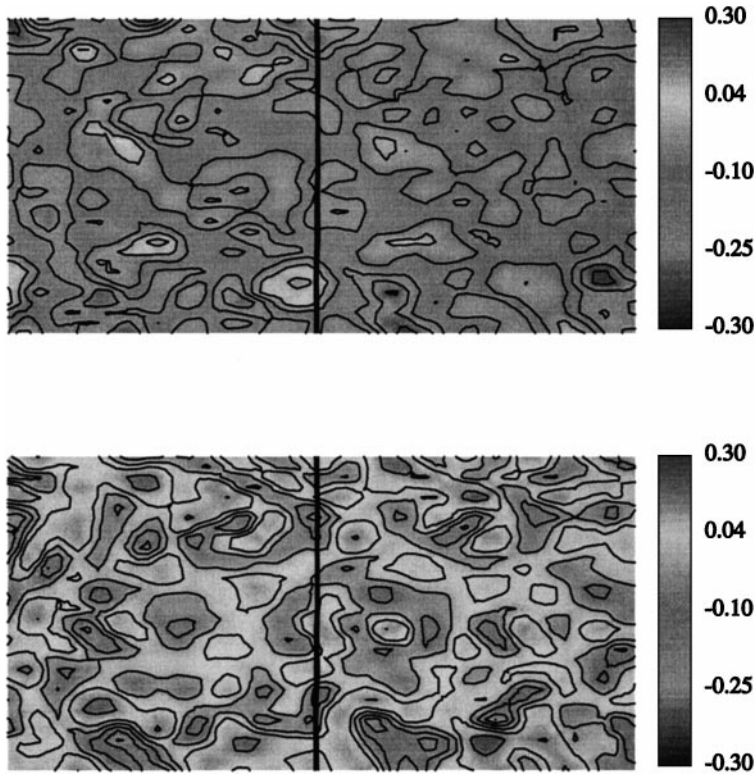

FIG. 25. Instantaneous cut of the streamwise ω_x (top) and of the transverse ω_z (bottom) vorticity field for simulation ST-1. Isopressure lines show the instantaneous position of the shock. Mean flow goes from left to right.

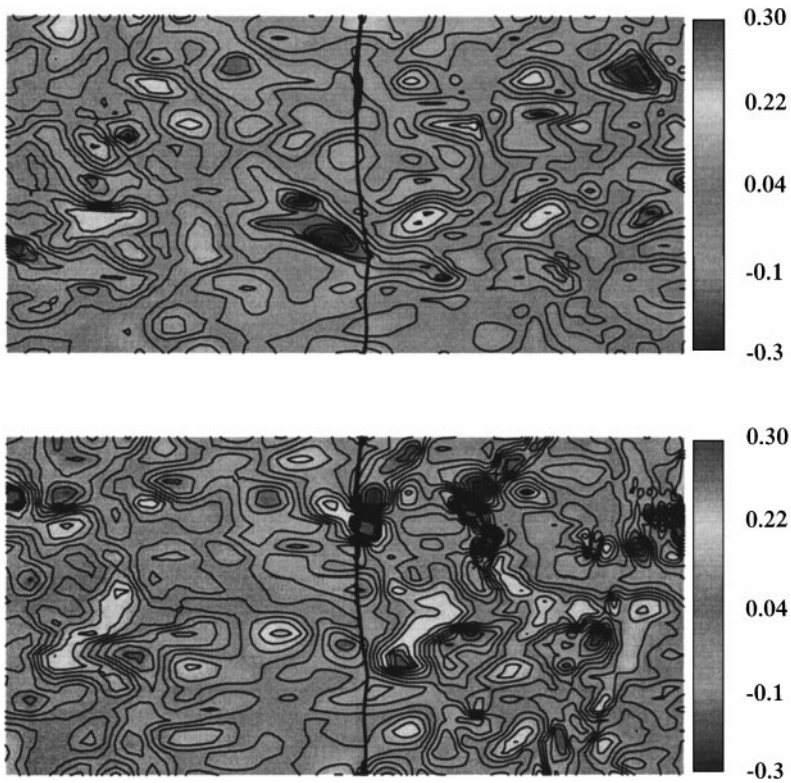

FIG. 26. Instantaneous cut of the streamwise ω_x (top) and of the transverse ω_z (bottom) vorticity field for simulation ST-4. Isopressure lines show the instantaneous position of the shock. The mean flow goes from left to right.

refinement takes place just before the shocked region, in a location that does not allow enough time for the convected turbulence to modify the range of scales contained in the turbulent motion. Should the grid refinement take place sooner, then the energy would cascade to smaller scales and cover all the spectrum available. This would generate enstrophy, following the same mechanism as the one seen in Subsection 4.1 and for the post-shock region in simulation ST-4. This effect is all the more intense here as the Reynolds number is infinite, but the same tendency is to be expected from all high Reynolds number applications. Two general procedures may improve the method: the first is the use of local automatic mesh refinement procedures (which would produce a quality of results equivalent to the ones obtained with ST-5) and the second is the use of pre-filtering procedures for LES. When pre-filtering the resolved fields to a chosen cut-off length scale larger than the characteristic width of the shock, no energetic scales of size about the width of the shock can enter the shock region and be dissipated by the second-order artificial viscosity.

6. CONCLUSION

We investigated the problem of high Reynolds number large-eddy simulations of the shock/turbulence interaction.

A skew-symmetric form of a finite volume Jameson type scheme of second-order accuracy was given. As the second- and fourth-order artificial dissipation terms involved in this type of schemes are too large to be applied with success for LES, the fourth-order artificial dissipation was suppressed (the LES model being able to get rid of small scales oscillations) and a new sensor based on the local property of compressibility of the flow was constructed.

This sensor allows the global scheme to capture the shock and to predict a right decay of turbulence kinetic energy in regions out of the shock. Moreover, the proposed sensor is shown to be frame independent, easy to implement in a parallel code, and relatively costless.

From a physical point of view, the simulations show the same trends as already published results for moderate Reynolds numbers. From a quantitative point of view, the increase of Reynolds stresses and vorticity fluctuations is slightly higher in our case than in former published results, which may be due to the absence of molecular viscosity and to the reduced numerical dissipation.

The necessity of grid refinement, already employed by [6], is shown to be directly connected with the ability to separate the smallest resolved scales of turbulence and the scales affected by the numerical dissipation used to capture the shock. This highlights the problem of simulating shock/turbulence interactions with energetic scales of sizes up to the cut-off length of the mesh L_{uvw} without encountering the problem of local decrease of the component of vorticity normal to the shock. This conclusion is taken from simulations using second order methods and may be modified when using higher order numerical schemes allowing a more accurate description of smallest resolved scales and shock corrugation.

REFERENCES

1. D. S. Dolling and C. T. Or, Unsteadiness of the shock wave structure in attached and separated compression ramp flows, *Exp. Fluids* **3**, 24 (1985).
2. J. Andreopoulos and K. C. Muck, Some new aspects of the shock-wave boundary layer interaction in compression ramp corner, *J. Fluid Mech.* **180**, 405 (1987).

3. A. J. Smits and K. C. Muck, Experimental study of three shock wave/turbulent boundary layer interactions, *J. Fluid Mech.* **182**, 294 (1987).
4. H. S. Ribner, *Convection of a Pattern of Vorticity through a Shock Wave*, NACA, Technical Note 2864 and Report 1164, 1953.
5. H. S. Ribner, Acoustic energy flux from shock-turbulence interaction, *J. Fluid Mech.* **35**, 299 (1969).
6. S. Lee, S. K. Lele, and P. Moin, Interaction of isotropic turbulence with shock waves: Effects of shock strength, *J. Fluid Mech.* **340**, 225 (1997).
7. S. Lee, S. K. Lele, and P. Moin, Direct numerical simulation of isotropic turbulence interacting with a weak shock wave, *J. Fluid Mech.* **251**, 533 (1993).
8. K. Mahesh, S. Lele, and P. Moin, The influence of entropy fluctuations on the interaction of turbulence with a shock wave, *J. Fluid Mech.* **334**, 353 (1997).
9. G. Erlebacher, M. Y. Hussaini, and C. W. Shu, Interaction of a shock with a longitudinal vortex, *J. Fluid Mech.* **337**, 129 (1997).
10. H. S. Ribner, Comments on experimental study of a normal shock/homogeneous turbulence interaction, *AIAA J.* **36**(3), 494 (1998).
11. S. Barre, D. Alex, and J. P. Bonnet, Reply by the authors to H. S. Ribner, *AIAA J.* **36**(3), 495 (1998).
12. C. Weber, Parallel implicit computation of turbulent transonic flow around a complete aircraft configuration, in *Parallel CFD 97 Conference, Manchester, 1997.*
13. R. Friedrich and R. Hannapel, Shock turbulence interaction, *Ercoftac Bull.* **34**, 34 (1997).
14. T. Soulères, *Schémas d'ordre élevé pour l'aérodynamique instationnaire: Etudes théoriques et implantation dans le code Navier-Stokes NSMB*, CERFACS Report No. STR/CFD/98/24, 1998.
15. D. Darracq and M. Gazaix, Computation of viscous shock/shock interaction with an upwind implicit scheme, in *Proceedings of the 19th International Symposium on Schock Waves* (Université de Provence Marseille, France, 1993).
16. E. David, *Modélisation des écoulements compressibles et hypersoniques: Une approche instationnaire*, Technical Report, Institut National Polytechnique de Grenoble, 1993.
17. P. Comte and M. Lesieur, Compressible shear flows in large-eddy simulation, *Ercoftac Bull.* **34**, 29 (1997).
18. D. H. Porter and P. R. Woodward, Numerical simulations of compressible convection, in *New Trends in Large Eddy Simulations* (Springer-Verlag, New York/Berlin, 1996).
19. S. O. Elaine and J. P. Boris, Computing turbulent shear flows- a convenient conspiracy, *Comput. Phys.* **7**(5), 523 (1993).
20. T. Passot and A. Pouquet, Numerical simulation of compressible homogeneous flows in the turbulent regime, *J. Fluid Mech.* **181**, 441 (1987).
21. E. Garnier, M. Mossi, P. Sagaut, P. Comte, and M. Deville, On the use of shock-capturing schemes for large-eddy simulation, *J. Comput. Fluid Dyn.*, in press.
22. L. Guichard, L. Vervisch, and P. Domingo, *Numerical Study of the interaction between a Mixing Zone and a Pressure Discontinuity*, AIAA Paper 95-0877, 33, 1995.
23. S. Lee, *Large Eddy Simulation of Shock Turbulence Interaction*, Center for Turbulence Research, Annual Research Briefs, Standford University, 1992.
24. P. Moin, K. Squires, W. Cabot, and S. Lee, A dynamic subgrid-scale model for compressible turbulence and scalar transport, *Phys. Fluids* **3**, 2746 (1992).
25. S. Ghosal, An analysis of numerical errors in large-eddy simulations of turbulence, *J. Comput. Phys.* **125**, 187 (1996).
26. A. G. Kravchenko and P. Moin, On the effect of numerical errors in large-eddy simulations of turbulent flows, *J. Comput. Phys.* **131**, 310 (1997).
27. R. Mittal and P. Moin, Suitability of upwind-biased finite difference schemes for large-eddy simulation of turbulent flows, *AIAA J.* **35**(8), 1415 (1997).
28. S. K. Lele, Compressibility effects on turbulence, *Ann. Rev. Fluid Mech.* **26**, 211 (1994).
29. G. Erlebacher, M. Y. Hussaini, C. G. Speziale, and T. A. Zang, Towards the large-eddy simulation of compressible turbulence, *J. Fluid Mech.* **238**, 155 (1992).

30. A. Yoshizawa, Statistical theory for compressible turbulent shear flows, with the application to subgrid modeling, *Phys. Fluids* **29**, 2152 (1986).
31. C. G. Speziale, G. Erlebacher, T. A. Zang, and M. Y. Hussaini. The subgrid-scale modeling of compressible turbulence, *Phys. Fluids* **31**, 940 (1988).
32. E. T. Spyropoulos and G. A. Blaisdell, *Evaluation of the Dynamic Subgrid-Scale Model for Large Eddy Simulations of Compressible Turbulent Flows*, AIAA Paper 95-0355, **33**(7), 1995.
33. F. Ducros, P. Comte, and M. Lesieur, Direct and large-eddy simulations of a supersonic boundary layer, in *Turbulent Shear Flow* 9 (Springer-Verlag, New York/Berlin, 1995).
34. P. Comte, Vortices in compressible LES and non-trivial geometries, *New tools in Turbulence Modelling*, edited by O. Métais and J. Ferziger, course of Ecole de Physique Théorique des Houches, France (Springer-Verlag, New York/Berlin, 1996).
35. M. V. Morkovin, Effects of compressibility on turbulent flows, in *Mécanique de la turbulence*, edited by A. Favre (1961), p. 367.
36. S. Sarkar, G. Erlebacher, M. Y. Hussaini, and H. O. Kreiss, The analysis and modelling of dilatational terms in compressible turbulence, *J. Fluid Mech.* **227** (1991).
37. F. Ducros, P. Comte, and M. Lesieur, Large-eddy simulation of a spatially growing boundary layer over an adiabatic flat plate, *Int. J. Heat Fluid Flow* **16**, 341 (1995).
38. F. Ducros, P. Comte, and M. Lesieur, Large-eddy simulation of transition to turbulence in a boundary layer spatially developing over a flat plate, *J. Fluid Mech.* **326**, 1 (1996).
39. M. Lesieur and O. Métais, New trends in large-eddy simulations of turbulence, *Ann. Rev. Fluid Mech.* **28**, 45 (1996).
40. M. Lesieur, "Turbulence in fluids," 2nd revised ed. (Kluwer Academic, Dordrecht, 1990).
41. J. Vos, E. Chaput, B. Arlinger, A. Rizzi, and A. Corjon, Recent advances in aerodynamics inside the nsmb (navier-stokes multi-block) consortium, in *36th Aerospace Sciences Meeting and Exhibit, Reno, NV, January 12–15, 1998*, AIAA-98-0802.
42. A. Jameson, W. Schmidt, and E. Turkel, *Numerical Solutions of the Euler Equations by Finite Volume Methods Using Runge-Kutta Time Stepping*, AIAA Paper 81-1250, 1981.
43. R. C. Swanson and E. Turkel, On central-difference and upwind schemes, *J. Comput. Phys.* **101**, 292 (1992).
44. H. J. Kaltenbach and H. Choi, *Large-Eddy Simulation of Flow around an Airfoil on a Structured Mesh*, Center for Turbulence Research, Annual Research Briefs, Standford University, 1995.
45. Y. Morinishi, *Conservative Properties of Finite Difference Schemes for Incompressible Flow*, Center for Turbulence Research, Annual Research Briefs, 1995.
46. P. L. Crumpton and G. J. Shaw, A vertex-centred finite volume method with shock detection, *Int. J. Numer. Method Fluids* **18**, 605 (1994).
47. R. Mittal, *Large-Eddy Simulation of Flow Past a Circular Cylinder*, Center for Turbulence Research, Annual Research Briefs, 1995.
48. G. Comte-Bellot and S. Corrsin, Simple eulerian time correlation of full- and narrow-band velocity signals in grid-generated, "isotropic" turbulence, *J. Fluid Mech.* **48**, 273 (1971).
49. O. Metais and M. Lesieur, Spectral large-eddy simulation of isotropic and stably stratified turbulence, *J. Fluid Mech.* **239**, 157 (1992).
50. E. Garnier, P. Sagaut, M. Mossi, P. Comte, and M. Deville, On the use of shock-capturing schemes for large-eddy simulation, in *Proceedings of ICFD Conference, 1998.*
51. H. Lamb, *Hydrodynamics* (Dover, New York, 1932).
52. P. Sagaut, E. Lenormand, and D. Klahr, *Poursuite du developpement du code pegase*, Rapport Technique No. RTS 18/4368 AY, 1996.
53. S. Lee, S. K. Lele, and P. Moin, Simulation of spatially evolving turbulence and the applicability of taylor hypothesis in compressible flow, *Phys. Fluids* **4**(7), 1521 (1992).
54. M. J. Lee, J. Kim, and P. Moin, Turbulence structure at high shear rate, *Turbulent Shear Flows* **6**, (1987).
55. S. Ghosal, *On the Large Eddy Simulation of Turbulent Flows in Complex Geometry*, Center for Turbulence Research, Annual Research Briefs, Standford University, 1993.
56. S. K. Lele, Shock-jump relations in a turbulent flow, *Phys. Fluid* **12**, 2900 (1992).